Master's thesis

NTNU
Norwegian University of Science and Technology
Faculty of Information Technology and Electrical Engineering
Department of Engineering Cybernetics

Ruben Kleiven

Robust and Gain Scheduled Flight Control of Fixed-wing UAVs in Wind and Icing Conditions

Master's thesis in Engineering Cybernetics
Supervisor: Tor Arne Johansen
Co-supervisor: Kristoffer Gryte
June 2021

NTNU
Norwegian University of Science and Technology

Ruben Kleiven

Robust and Gain Scheduled Flight Control of Fixed-wing UAVs in Wind and Icing Conditions

Master's thesis in Engineering Cybernetics
Supervisor: Tor Arne Johansen
Co-supervisor: Kristoffer Gryte
June 2021

Norwegian University of Science and Technology
Faculty of Information Technology and Electrical Engineering
Department of Engineering Cybernetics

NTNU
Norwegian University of
Science and Technology

Abstract

Inspired by the growing field of application of unmanned aerial vehicles (UAVs), this thesis investigates robust and gain scheduled flight control of fixed-wing UAVs in wind and icing conditions. The motivation for this work is to generate a set of controllers that overcomes the difficulties related to plant uncertainties, atmospheric in-flight icing and wind disturbances.

The main objective is to develop controllers that mitigate the aerodynamic effects of wind and icing on the UAV. However, several intermediate steps are completed to create and test these controllers. Specifically, a simulation software package in Python is developed to perform system analysis, controller tuning and numerical simulations. A thorough dynamic mode analysis is made to compare the icing-induced changes of the dynamic system to the basic clean UAV. An asymmetric aircraft model is deduced from symmetrical data to perform lifelike simulations related to de-icing. At last, the controller is implemented using a systematic loop-shaping procedure and tested in the simulation environment.

The controller methods are based on $\mathcal{H}_\infty$ control approach and using a systematic loop-shaping design procedure for tuning. The control methods were tested through numerical simulations using the developed software package. From these simulations, it is concluded that both the single robust controller and the gain scheduled controller gives satisfactory results in terms of stability, robustness and performance. However, by comparing the results from the performance test runs for the two controllers, the control performance of the gain-scheduled control approach gives better results. This result proves that one can improve the controller performance while fulfilling the closed-loop robustness and stability requirements by including knowledge of icing.

In-flight de-icing is performed using the single robust controller for different levels of airspeed. The tendency is clear; higher airspeed within the tested range of reasonable UAV airspeeds minimizes the disturbance related to instantaneous removal of ice.

Sammendrag

Inspirert av de stadig voksende bruksområdene for droner, fokuserer denne oppgaven på robust og "gain scheduled" regulering av fastvingedroner i vind- og isforhold. Hovedmålet for dette arbeidet er å generere et sett med regulatorer som løser vanskeligheter knyttet til modellusikkerhet, atmosfærisk ising og vindforstyrrelser. Flere mellomtrinn utført i denne prosessen. En programvarepakke i Python er utviklet for å utføre systemanalyse, regulator tuning og numeriske simuleringer. En grundig egenverdianalyse er utført for å sammenligne de isdannede endringene i det dynamiske systemet med den ordinære dronen uten is. I tillegg er en asymmetrisk flymodell utledet fra symmetriske data for å utføre virkelighetsreelle simuleringer relatert til avisning. Til slutt er regulatorene utviklet og testet i simulatoren.

Regulatormetodene er basert på $\mathcal{H}_\infty$ regulering, og bruker en systematisk tune-prosedyre for tuning. Regulatorene ble testet gjennom numeriske simuleringer ved hjelp av den nevnte programvaren. Fra denne simuleringen kan det konkluderes med at både den enkle robuste regulatoren og "gain scheduled" regulatoren gir tilfredsstillende resultater når det gjelder stabilitet, robusthet og ytelse. Ved å sammenligne resultatene fra ytelsestestene for de to regulatorene, gir regulatorytelsen til "gain scheduled" regulatoren de beste resultatene. Dette viser at man kan forbedre regulatorens ytelse mens man følger definerte lukket sløyfe robusthets- og stabilitetskrav ved å inkludere kunnskap om isingsnivået.

En avisingsprosess er simulert for den enkle robuste regulatoren ved forskjellige vindhastigheter. Her er tendensen klar; høyere vindhastighet minimerer forstyrrelsene relatert til momentan avising.

Preface

This thesis is a part of the course TTK4900 master's thesis in Engineering Cybernetics at the Norwegian University of Science and Technology (NTNU). The work presented in this thesis is performed at the Department of Engineering Cybernetics.

The starting point of this task was to investigate the control of a UAV that is subject to wind and icing conditions. The aerodynamic models of the Skywalker X8 were given from previous work and analysis. This work is a continuation of the work presented in my pre-master project [1]. The pre-master project investigated linear control of non-linear plants with uncertainties. Parts of the same control approaches are applied in this thesis. However, the control problem is extended to include more complex and life-like simulation test scenarios related to wind and icing conditions in this thesis. This has increased the focus on disturbance rejection for the controller designs.

I would like to thank my main supervisor, Professor Tor Arne Johansen and Co-supervisor Kristoffer Gryte for their help and guidance throughout this project. Their ideas and support have been very valuable during the work with this thesis.

Contents

List of Tables

List of Figures

Part I

Introduction and Background Material

Chapter 1

Introduction

The application areas for Unmanned aerial vehicles (UAVs) have extensively increased throughout the past decades. UAVs have already proven helpful in military-, scientific- and civil applications. The increasing use has led to higher requirements when it comes to tolerance of flying UAVs in rough conditions. This thesis focuses on control of UAVs in icing and wind conditions.

In aviation, icing conditions are potentially dangerous and has been an essential factor in numerous accidents. Icing may occur when an aircraft is on the ground or airborne. For airborne aircraft, in-flight air-frame icing, also known as atmospheric icing, occurs when super-cooled water droplets in clouds freeze on impact with the aircraft surface. This is the type of icing considered throughout this thesis.

There are primarily two approaches to avoid/limit icing conditions, namely preventive anti-icing and corrective de-icing. According to Thomas *et al.* [2], these two approaches can be divided into three groups, freezing point depressants, thermal melting and surface deformation. When looking at avoiding and limiting icing conditions, there is a distinction between large aircraft and smaller UAVs. UAVs has significantly higher requirements when it comes to energy consumption and loading weight. This can make some de-icing and anti-icing techniques less convenient for UAVs.

When de-icing in-flight, it is likely that the amount of ice on each wing is considerably different for a small amount of time. Having a partly defect de-icing system, where it only works on one of the wings is also a possible scenario. This motivates for extending the symmetric model in [3] into an asymmetric model.

In order to fly an aircraft, the flight control system is normally divided into two levels [4]; a low-level control system that stabilizes the airframe using available sensor measurements and actuators and a higher-level outer guidance control loop. Since this thesis focuses on the stability and performance affection of wind and icing conditions, only the inner-loop

controller is considered.

1.1 Previous Work

Not surprisingly, UAV and aircraft control is well covered in the literature. Linear control methods are commonly used in textbooks that covers UAV control [5–7]. Here, a linearized approximation of the system dynamics is used to obtain controllers from state-space control design methods. Several control methods, e.g. linear quadratic regulator (LQR) and $\mathcal{H}_\infty$-optimal control are proposed by Lavretsky and Wise [6]. Beard and Mclain [5] use a simple PID-autopilot design for both guidance and control.

The specific UAV used in this thesis is the Skywalker X8. The previous modelling work done by Gryte *et al.* [8] and Winter [3] makes a model-based controller design approach convenient. This motivates developing a simulation environment where it is possible to perform comprehensive system analysis.

Icing effects on aircraft performance has also been a subject of research throughout the last decades ([9–15]). Generally, icing affects the smooth flow of air, increases the drag force and weight and decreases the ability of the airfoil to lift. A study performed by Hann [16], also showed that these performance penalties caused by icing conditions is greater on UAVs than on larger manned aircraft.

Controlling aircraft with asymmetry is caused by wing damage or actuator failure is done by Chowdhary *et al.* [17]. Here, both model reference adaptive control (MRAC) and a linear proportional-integral– derivative (PID)-type attitude controller is used for inner-loop control.

1.2 Contributions

The thesis aims to develop controllers to achieve robust stability and performance in icing and wind conditions. Based on this, the following contributions are made;

- Flight Control Analysis Toolbox (FCAT) [18], which is a software package in python made for simulating and analyzing flying rigid bodies.
- Dynamic mode analysis on the effects of icing conditions.
- Deducing an asymmetric aircraft model from only symmetric model data.
- Systematic loop-shaping design procedure for $\mathcal{H}_\infty$-optimal controller. The loop-shaping design procedure is based tuning methods used in the pre-master project [1].

1.3 Structure of Thesis

The thesis is divided into three parts;

- Part one consists of two chapters, namely introduction and theoretical framework. The theoretical framework chapter presents the theory used in the subsequent chapters. This includes UAV modelling concepts, wind gusts model and control techniques.
- Part 2 consists of chapter 3, 4, 5 and 6. Chapter 3 describes the simulation software, chapter 4 introduces the specific Skywalker X8 model, chapter 5 presents the controller tuning process and chapter 6 describes the simulation scenarios.
- Part 3 consists of chapter 7, 8 and 9. The results are presented in chapter 7. Chapter 8 and 9 are the discussion and conclusion chapters.

Chapter 2

Theoretical Framework

This chapter provides basic theory and background information needed to comprehend the material introduced throughout this thesis. This includes modelling an aircraft, the Dryden wind turbulence model, $\mathcal{H}_\infty$ robust control and gain-scheduled control.

2.1 Modelling the UAV

This section will give the outlines of the derivation of the mathematical model used in simulations. More detailed derivations can be found in most flight dynamics textbook [5, 6, 19].

2.1.1 Reference Frames

Different frames of reference are used in order to describe the motion of the UAV. A space-fixed reference frame is suitable for long term guidance, where the equations of motion are most easily expressed in a body-fixed reference frame. The different frames of reference used here are the world reference frame, the body frame and the wind frame.

The world reference frame denoted $\mathcal{F}^i$ uses the North, East, Down (NED)-convention. The origin is located at a fixed point on Earth. The x-axis points north, the y-axis points east, and the z-axis points down into the Earth's centre.

The body frame denoted $\mathcal{F}^b$ has its origin at the centre of mass (COM) of the UAV. Here, the x-axis points out of the aircraft's nose, the y-axis points along with the right-wing, and the z-axis points out of the aircraft's belly. The orientation of the body frame with respect to the aircraft is visualized in figure 2.2. Note that the origin is, as mentioned, located in the COM.

The wind frame denoted $\mathcal{F}^w$ has its origin at the COM of the aircraft, and the axes are oriented based on the aircraft's motion relative to the surrounding wind. This frame can

be obtained by rotating the body frame by the rotation described by figure 2.1. The wind frame is obtained by first rotating the x^b and z^b axes the angle of attack, α, about the y^b-axis followed by rotating the y^b-axis and new x-axis the angle of sideslip about the z^w-axis. This rotation is described by the rotation matrix in equation A.2. Now, the x^w-axis points in the direction of the airspeed, $\mathbf{V_a}$.

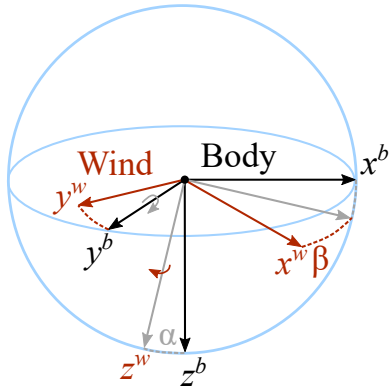

Figure 2.1: Rotations from body frame to wind frame.

2.1.2 Aircraft Flight Dynamics Equations of Motion

As mentioned in section 2.1.1, the equations of motion are most easily expressed in a body frame. These dynamics can be obtained by using Newton's second law of motion. The motion of the UAV (treated as a rigid body) is comprised of three translational and three rotational degrees of freedom.

The transnational motion can be described by the velocity vector, $\mathbf{V} = [u, v, w]$, where u, v and w hare the forward, lateral and vertical velocities given in the body frame. The rotational motion can be described by the angular rates vector, $\boldsymbol{\omega} = [p, q, r]$, where p, q and r are the body roll, body pitch and body yaw rates. Now, by representing the sum of all external forces acting on the rigid body as $\mathbf{F}$, and the sum of all external moments about the centre of mass as $\mathbf{M}$, we get the following equations;

$$\begin{aligned} m(\dot{\boldsymbol{V}} + \boldsymbol{\omega} \times \boldsymbol{V}) &= \boldsymbol{F} \\ \boldsymbol{I}\dot{\boldsymbol{\omega}} + \boldsymbol{\omega} \times \boldsymbol{I}\boldsymbol{\omega} &= \boldsymbol{M} \end{aligned} \tag{2.1}$$

Where $\mathbf{I}$ is the inertia matrix. $\mathbf{F}$ and $\mathbf{M}$ are primarily from three sources, namely gravitation, propulsion and aerodynamic [5]. This is mathematically expressed in equation 2.2.

$$\begin{aligned} \mathbf{F} &= \mathbf{F}_a + \mathbf{F}_g + \mathbf{F}_p \\ \mathbf{M} &= \mathbf{M}_a + \mathbf{M}_p + \mathbf{M}_g \end{aligned} \tag{2.2}$$

Where subscript g, p and a denotes gravitational, propulsion and aerodynamic forces respectively. These forces and moments are described in sections 2.1.3, 2.1.4 and 2.1.5.

The Euler angles are denoted as $\boldsymbol{\Theta} = [\phi, \theta, \psi]$. Here, ϕ is the roll angle, θ is the pitch angle, and ψ is the yaw angle. These angles give the inertial angular rotation of the aircraft. The kinematic relation in equation 2.3 describes the dynamics of the Euler angles as a function of the angular rates in body frame [6].

$$\dot{\Theta} = \begin{bmatrix} 1 & sin(\phi)tan(\theta) & cos(\phi)tan(\theta) \\ 0 & cos(\phi) & -sin(\phi) \\ 0 & sin(\phi)sec(\theta) & cos(\phi)sec(\theta) \end{bmatrix} \boldsymbol{\omega} \tag{2.3}$$

The inertial position, $\mathbf{P} = [p_n, p_e, p_d]$, is the north, east and altitude coordinates are given in the world reference frame. Note that $p_d = -h$, where h is the height above ground. The relation between the inertial velocities, $\dot{\mathbf{P}}$ and the body frame velocity $\mathbf{V}$ are given by equation 2.4, which in essence are rotating the body-fixed velocity vector from the body frame to world reference frame.

$$\dot{\mathbf{P}} = \mathbf{R}_b^i(\phi, \theta, \psi)\boldsymbol{V} \tag{2.4}$$

Where $\mathbf{R}_b^i(\phi, \theta, \psi)$ is the rotational matrix from body to inertial frame, given by equation A.1. By combining the equations of motion in equation 2.1 with the relations in equations 2.3 and 2.4, a twelve state model with state vector $\boldsymbol{x} = [p_n, p_e, p_d, \phi, \theta, \psi, u, v, w, p, q, r]$ is obtained.

2.1.3 Aerodynamic Forces and Moments

The aerodynamic forces consist of drag-, side- and lift forces, and are denoted F_D, F_S and F_L respectively. These forces most easily modeled in the wind frame, and need to be rotated into body frame before they are applied in equation 2.2. The aerodynamic forces in body frame are given by equation 2.5.

$$\boldsymbol{F}_a = \begin{bmatrix} F_x \\ F_y \\ F_z \end{bmatrix} = \mathbf{R}_w^b(\alpha, \beta) \begin{bmatrix} -F_D \\ F_S \\ -F_L \end{bmatrix} \tag{2.5}$$

Where $\mathbf{R}_w^b(\alpha, \beta)$ is the rotation matrix from wind frame to body frame and can be found by taking the transpose of the rotation matrix from body frame to wind frame in equation A.2. The drag and lift forces act along the negative z^w and x^w axes, which explains the negative signs.

The aerodynamic forces and moments are typically modelled as dimensionless functions. A common simplification is to separate the aerodynamic functions into longitudinal ($\mathbf{x_b}$-$\mathbf{z_b}$ plane) and lateral direction ($\mathbf{x_b}$-$\mathbf{y_b}$- plane) [5]. l, m, n are the aerodynamic moments about body-frame x,y and z axes. Then, by denoting V_a as the airspeed of the aircraft, S as the area of the wing, b as the wingspan of the aircraft and c as the mean chord of the wing, the aerodynamic forces and moments in the longitudinal direction can be written as in equation 2.6.

$$\begin{bmatrix} F_D \\ F_L \\ m \end{bmatrix} = \frac{1}{2}\rho V_a^2 S \begin{bmatrix} C_D(\alpha, q, \delta_e) \\ C_L(\alpha, q, \delta_e) \\ cC_{\mathrm{m}}(\alpha, q, \delta_e) \end{bmatrix} \tag{2.6}$$

The lateral direction aerodynamic forces and moments can be expressed as in equation 2.7.

$$\begin{bmatrix} F_S \\ l \\ n \end{bmatrix} = \frac{1}{2}\rho V_a^2 S \begin{bmatrix} C_Y(\beta, p, r, \delta_a, \delta_r) \\ bC_{\mathrm{l}}(\beta, p, r, \delta_a, \delta_r) \\ bC_{\mathrm{n}}(\beta, p, r, \delta_a, \delta_r) \end{bmatrix} \tag{2.7}$$

Where C_D, C_Y and C_L, are non-dimensional drag-, side- and lift force functions, and C_l, C_m and C_n are non-dimensional are rolling-, pitching- and yawing moment functions. The differential aileron angle δ_a, the elevator angle δ_e and the rudder angle δ_r are the primary control surfaces, and are used to control roll-, pitch- and yaw motion respectively. By combining equations 2.5, 2.6 and 2.7, the aerodynamic forces and moments can be summarized as;

$$\begin{aligned} \boldsymbol{F}_a &= \begin{bmatrix} F_x \\ F_y \\ F_z \end{bmatrix} = \mathbf{R}_w^b(\alpha, \beta)\frac{1}{2}\rho V_a^2 S \begin{bmatrix} -C_D(\alpha, q, \delta_e) \\ C_Y(\beta, p, r, \delta_a, \delta_r) \\ -C_L(\alpha, q, \delta_e) \end{bmatrix} \\ \boldsymbol{M}_a &= \begin{bmatrix} l \\ m \\ n \end{bmatrix} = \frac{1}{2}\rho V_a^2 S \begin{bmatrix} bC_{\mathrm{l}}(\beta, p, r, \delta_a, \delta_r) \\ cC_{\mathrm{m}}(\alpha, q, \delta_e) \\ bC_{\mathrm{n}}(\beta, p, r, \delta_a, \delta_r) \end{bmatrix} \end{aligned} \tag{2.8}$$

2.1.4 Gravitational Forces and Moments

For a rigid symmetric aircraft, the gravitational moment about the center of mass is 0. This implies that $\boldsymbol{M}_g = 0$. The gravitational force acting on the aircraft can be written as $\boldsymbol{F}_g^i = [0, 0, mg]$ in the world reference frame, where m is the mass of the aircraft and g is the acceleration of gravity. The gravitational force in body frame is therefore written as;

$$\boldsymbol{F}_g = \boldsymbol{R}_i^b \boldsymbol{F}_g^i \tag{2.9}$$

Where $\boldsymbol{R}_i^b$ is found by taking the transpose of the rotation matrix $\boldsymbol{R}_b^i$ in equation A.1.

2.1.5 Propulsion Forces and Moments

A non-complex model for propulsion can be obtained by applying Bernoulli's equation to the air in front of and behind the propeller [5]. By making the assumptions that the thrust force generated is directly along the x-axis of the body frame, the relation between throttle to exit velocity is linear and that the propeller efficiency is constant, the thrust force is

given in equation 2.10.

$$\mathbf{F_P} = \frac{1}{2}\rho S_{\text{prop}} C_{\text{prop}} \begin{bmatrix} (k_{\text{motor}}\delta_t)^2 - V_a^2 \\ 0 \\ 0 \end{bmatrix} \tag{2.10}$$

Where S_{prop} is the area swept out by the propeller, C_{prop} is an efficiency factor and k_{motor} is the motor constant.

2.1.6 Asymmetric Aircraft Model

In this section, an asymmetric aircraft model is deduced from symmetric data. All forces in equation 2.8 are acting through the aircraft centre of mass. Similarly, all moments are acting about the aircraft centre of mass. An asymmetric aircraft model is obtained by dividing the aircraft into two parts, a left side and a right side. This thesis is only considering asymmetry in aerodynamic forces and moments, but the same principles can, in theory, be applied for gravitational and propulsion forces and moments as well. Figure 2.2 illustrates this division and shows new decoupled aerodynamic forces. The forces acting on the right-wing are denoted $\boldsymbol{F}_{k,r}$, where k can be D, S or L for drag-, side- and lift force, respectively. The forces acting on the left-wing are denoted $\boldsymbol{F}_{k,l}$. The distance vector from the centre of mass to the point of attack on the right-wing is denoted $\boldsymbol{r}_k$. By using the right-wing drag force, $\boldsymbol{F}_{D,r}$ as an example, the distance vector from the centre of mass to the point of attack is denoted $\boldsymbol{r}_D$. Similarly, the distance vector from the centre of mass to a force acting on the left wing is denoted $\boldsymbol{l}_k$.

The drag-, side- and lift forces acting through the aircraft centre of mass described in section 2.1.3 is now given by a sum of the two corresponding forces on each wing, as shown in equation 2.11.

$$\boldsymbol{F}_k = \boldsymbol{F}_{k,r} + \boldsymbol{F}_{k,l} \tag{2.11}$$

A similar relation can be written for the for the moments. The aerodynamic moment is now given by equation 2.12.

$$\boldsymbol{M}_{a,\text{asym}} = \boldsymbol{M}_{a,0} + \sum_k (\boldsymbol{r}_k \times \boldsymbol{F}_{k,r} + \boldsymbol{l}_k \times \boldsymbol{F}_{k,l}) \text{ for } \boldsymbol{F}_{k,r}, \boldsymbol{F}_{k,l} \notin \boldsymbol{M}_{a,0} \tag{2.12}$$

Where $\boldsymbol{M}_{a,0}$ is the symmetric moment vector from equation 2.8. The second term is caused by asymmetry in corresponding aerodynamic forces on the left and right wing. Note that in order to avoid counting the force contribution twice, the last term is only added if they are not already taken into account as a part of the symmetric case.

2.2 Modelling Wind Gusts

Wind gust models are used for simulating the UAV in more realistic environments. Two of the most common continuous wind gust models are the Dryden model and the Von Karman model. The Dryden model, which will be used in this thesis, is an approximation of the

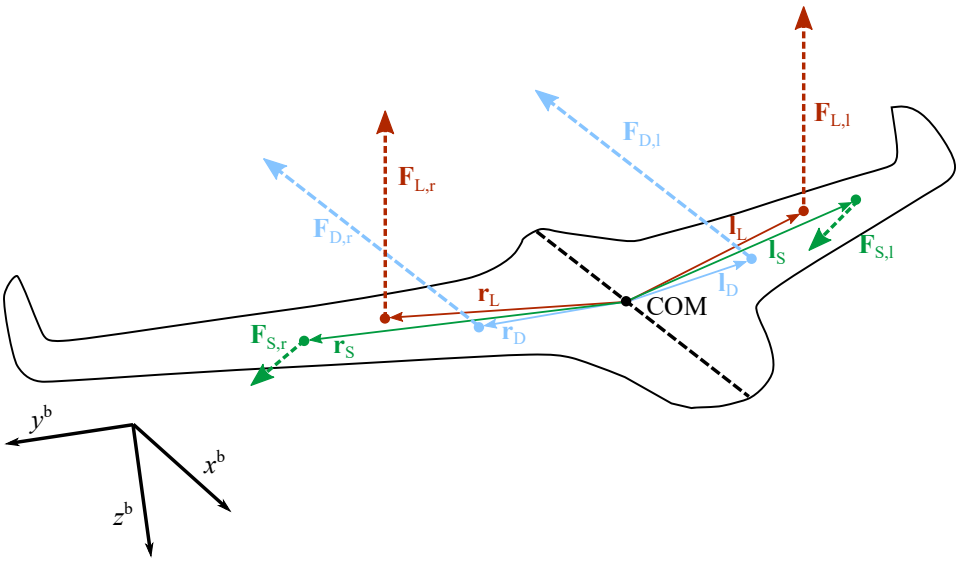

Figure 2.2: Asymmetric forces aircraft model

von Karmen model and is briefly described in Beard and McLain [5]. The Dryden model is a stochastic process described by six coloring filters; H_u, H_v and H_w is describing the wind effect on translational velocity u, v and w, and H_p, H_q and H_r describing the wind effect on rotational wind velocities p, q and r. By using the mathematical representation given by the military specification MIL-F-8785C in [20], these filters are given by equation 2.13 [21].

$$
\begin{aligned}
H_u(s) &= \sigma_u \sqrt{\frac{2L_u}{\pi V_a}} \frac{1}{1+\frac{L_u}{V_a}s} \\
H_v(s) &= \sigma_v \sqrt{\frac{L_v}{\pi V_a}} \frac{1+\frac{\sqrt{3}L_v}{V_a}s}{(1+\frac{L_v}{V_a}s)^2} \\
H_w(s) &= \sigma_w \sqrt{\frac{L_w}{\pi V_a}} \frac{1+\frac{\sqrt{3}L_w}{V_a}s}{(1+\frac{L_w}{V_a}s)^2} \\
H_p(s) &= \sigma_w \sqrt{\frac{0.8}{V_a}} \frac{(\frac{\pi}{4b})^{\frac{1}{6}}}{L_w^{\frac{1}{3}}(1+\frac{4b}{\pi V_a}s)} \\
H_q(s) &= \frac{-\frac{s}{V_a}}{(1+\frac{4b}{\pi V_a}s)} H_w(s) \\
H_r(s) &= \frac{\frac{s}{V_a}}{(1+\frac{3b}{\pi V_a}s)} H_v(s)
\end{aligned}
\tag{2.13}
$$

Here, σ_u, σ_v and σ_w are the turbulence intensities, L_u, L_v and L_w are the turbulence scale lengths, b is the wingspan and V_a is the airspeed. Wind gusts are then obtained by passing

white noise through these filters. The parameter values in equation 2.13 for altitudes below 1000 feets are given by [20], and shown in 2.14.

$$\begin{aligned} \sigma_w &= 0.1V_{20} \\ \sigma_u &= \sigma_v = \frac{1}{(0.177 + 0.000823h)^{0.4}} \\ L_u &= L_v = \frac{h}{(0.177 + 0.000823h)^{1.2}} \\ L_w &= h \end{aligned} \tag{2.14}$$

V_{20} is the wind speed at 20 feet dependant on intensity. Typical values for low, moderate and severe intensities are 15, 30 and 45 knots [20].

2.3 $\mathcal{H}_\infty$ Optimal Control

$\mathcal{H}_\infty$ optimal controller can be found by formulating the control problem as a mathematical optimization problem. This section gives the outlines regarding problem formulation and tuning process used in $\mathcal{H}_\infty$ optimal control. More detailed descriptions are given in [6, 22, 23].

2.3.1 Problem Formulation

The standard problem formulation commonly used for $\mathcal{H}_\infty$ control are shown in figure 2.3 [23]. Here, $\boldsymbol{u}$ is the control variables, $\boldsymbol{y}$ is the measured variables, $\boldsymbol{z}$ is the weighted error signals which are to be minimized, and $\boldsymbol{w}$ is the exogenous inputs, including disturbances, sensor noise and reference signals. $\boldsymbol{P}$ is the general plant and $\boldsymbol{C}$ is the feedback controller.

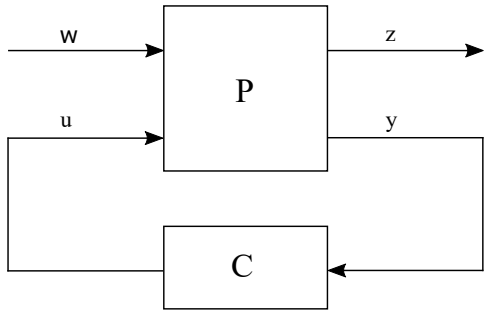

Figure 2.3: General Control Configuration

The state-space equations for a general linearized process with system states, $\boldsymbol{x}$, is written

in equation 2.15.

$$\begin{aligned}\dot{\mathbf{x}} &= \mathbf{A}\mathbf{x} + \mathbf{B}\mathbf{u} + \mathbf{E}\mathbf{w} \\ \mathbf{z} &= \mathbf{C}_1\mathbf{x} + \mathbf{D}_2\mathbf{u} + \mathbf{D}_1\mathbf{w} \\ \mathbf{y} &= \mathbf{C}_2\mathbf{x} + \mathbf{D}_4\mathbf{u} + \mathbf{D}_3\mathbf{w}\end{aligned} \tag{2.15}$$

The transfer function of this process, $\boldsymbol{P}(s)$ in figure 2.3, is given by equation 2.16.

$$\begin{aligned}\mathbf{P}(s) &= \begin{bmatrix} \mathbf{D}_1 & \mathbf{D}_2 \\ \mathbf{D}_3 & \mathbf{D}_4 \end{bmatrix} + \begin{bmatrix} \mathbf{C}_1 \\ \mathbf{C}_2 \end{bmatrix} (s\boldsymbol{I} - \boldsymbol{A})^{-1} \begin{bmatrix} \mathbf{E} & \mathbf{B} \end{bmatrix} \\ &= \left[\begin{array}{c|c} \mathbf{P}_{11} & \mathbf{P}_{12} \\ \hline \mathbf{P}_{21} & \mathbf{P}_{22} \end{array}\right]\end{aligned} \tag{2.16}$$

For a linear controller, $\mathbf{C}(s)$, connected from $\boldsymbol{y}$ to $\boldsymbol{u}$, as shown in figure 2.3, the closed loop transfer function from exogenous inputs to the weighted error signal is given by equation 2.17 [24].

$$\frac{\mathbf{z}}{\mathbf{w}}(s) = \mathcal{F}(\mathbf{P}, \mathbf{C})(s) = \mathbf{P}_{11} + \mathbf{P}_{12}\mathbf{C}(\mathbf{I} - \mathbf{P}_{22}\mathbf{C})^{-1}\mathbf{P}_{21} \tag{2.17}$$

The $\mathcal{H}_\infty$ optimized controller seeks to minimize the worst case effects of the exogenous inputs $\mathbf{w}$ on the weighted error signal $\mathbf{z}$. This is done by minimizing the infinity norm of the transfer function $\mathcal{F}(\mathbf{P}, \mathbf{C})(s)$. By denoting the maximum singular value as $\bar{\sigma}(\cdot)$, the infinity norm is given by the expression in equation 2.18.

$$||\mathcal{F}(\mathbf{P}, \mathbf{C})(s)||_\infty = \sup_\omega \bar{\sigma}(\mathcal{F}(\mathbf{P}, \mathbf{C})(j\omega)) \tag{2.18}$$

2.3.2 Controller Tuning

The tuning parameters of the $\mathcal{H}_\infty$ controller are the weighting filters used on the error signals $\boldsymbol{z}$. By denoting the model plant as $\boldsymbol{G}(s)$, the sensitivity function $\boldsymbol{S}(s)$ and complementary sensitivity function $\boldsymbol{T}(s)$ are defined as;

$$\begin{aligned}\boldsymbol{S}(s) &= (\boldsymbol{I} + \boldsymbol{L}(s))^{-1} \\ \boldsymbol{T}(s) &= \boldsymbol{L}(\boldsymbol{I} + \boldsymbol{L}(s))^{-1}\end{aligned} \tag{2.19}$$

Where $\boldsymbol{L}(s) = \boldsymbol{G}(s)\boldsymbol{C}(s)$ is the open loop transfer function, and $\boldsymbol{I}$ is the identity matrix of the same order as $\boldsymbol{L}(s)$.

Figure 2.4 shows a block diagram of the system with weighting filters, where W_S, W_C and W_T are weighting filters and z_1, z_2 and z_3 are the weighted sensitivity, control activity and complementary sensitivity. The transfer function from reference $\mathbf{r}$ to the error $\boldsymbol{e}(s)$ and measured output $\boldsymbol{y}(s)$ is given by equation 2.20.

$$\begin{aligned} \boldsymbol{e}(s) &= \boldsymbol{S}(s)\boldsymbol{r}(s) \\ \boldsymbol{y}(s) &= \boldsymbol{T}(s)\boldsymbol{r}(s) \end{aligned} \tag{2.20}$$

The error-signals z_1 and z_3 are the weighted sensitivity and complementary sensitivity, and z_2 is the weighted control activity. To ensure good reference tracking, it is desirable to have a high complementary sensitivity gain and low sensitivity gain at low frequencies. At high frequencies, it is desirable to have a low complementary sensitivity gain to ensure good noise attenuation and robustness.

There are multiple methods to design weighting filters. The two most common methods are the signal-based approach used in Doyle et al. [25] and loop-shaping. The signal-based approach is a very general method that evaluates the response to sinusoidal signals. This method is more appropriate for multi-variable problems in which several objectives need to be taken into account simultaneously [23]. For this reason, this thesis is using a loop-shaping approach, which is thoroughly described in Lavretsky et al. [6]. Here, the weighting filters are used to shape the desired sensitivity and complementary sensitivity frequency responses. In order to avoid unnecessary complex controllers, the weighting filters should be chosen of the lowest order that meets the desired requirements [6]. The transfer functions are limited by the inverse of its corresponding filter. By using the sensitivity function as an example, W_s should be the inverse of the desired shape of $\boldsymbol{S}(s)$, such that when the infinity norm of the error signal, here $z_1 = ||W_S S||_\infty$, is minimized, it will shape the desired $\boldsymbol{S}(s)$.

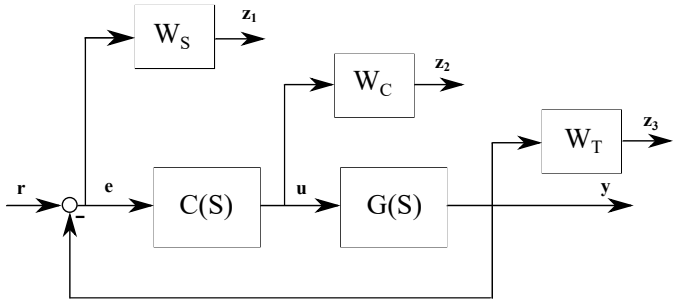

Figure 2.4: Closed-loop block diagram with weighted error signals.

2.3.3 γ-iteration

γ-iteration is a bisection algorithm used to find $\mathcal{H}_\infty$ optimized controller. The γ-iteration method starts with high, γ_{max}, and low, γ_{min}, estimates of γ and iterates on γ-values to find the $\mathcal{H}_\infty$ optimal controller. There are numerical methods used for solving the $\mathcal{H}_\infty$-problem. For the Riccati-based method used in Lavertsky *et al.* [6], this algorithm computes the smallest γ-value, γ_{opt}, within the γ-range for which the stabilizing non-negative definite Riccati-solutions exists. Now, γ_{opt} is the controller performance level, and the following relation is met;

$$||\mathcal{F}(\mathbf{P}, \mathbf{C})(s)||_\infty < \gamma_{\text{opt}} \tag{2.21}$$

2.4 Robust Stability

This section provides the techniques used to investigate robust stability for single-input single-output (SISO) systems.

2.4.1 Vinnicombe Distance

The Vinnicombe metric, denoted as ν-gap metric, is a distance measure between two linear time-invariant (LTI) systems. A detailed description of the ν-gap metric can be found in [22, 26, 27]. Aircraft in icing condition can be handled as a nominal plant with plant uncertainty. Hence the ν-gap metric can be used as an uncertainty measure between the nominal plant and the plant at a given icing level.

The winding number condition for two scalar LTI systems, P_1 and P_2, is given by equation 2.22.

$$(1 + P_2^* P_1) \neq 0 \forall \omega \tag{2.22a}$$

$$\text{wno}(1 + P_2^* P_1) + \eta(P_1) - \eta(P_2) - \eta_0(P_2) = 0 \tag{2.22b}$$

Where the winding number, wno, is evaluated along the standard Nyquist contour, $\eta(\cdot)$ denotes the number of unstable poles, $\eta_0(\cdot)$ is the number of poles on the imaginary axis and P_i^* is the conjugated plant P_i (takes $P_i(s)$ to $P_i(-s)$). By denoting the set of all LTI system pairs, (P_1, P_2), that fullfills the condition in equation 2.22 as $\mathcal{S}$, the Vinnicombe distance is defined by equation 2.23.

$$\delta_v(P_1, P_2) = \begin{cases} \sup_\omega \frac{|P_1 - P_2|}{\sqrt{(1+P_1 P_1^*)(1+P_2 P_2^*)}}, \text{if} (P_1, P_2) \in \mathcal{S} \\ 1, \text{otherwise} \end{cases} \tag{2.23}$$

Since the LTI systems considered in this thesis are all scalar systems, equations 2.22 and 2.23 are simplified to yield scalar functions.

2.4.2 Gap Metric Stability Margin

The gap metric stability margin, also known as normalized coprime stability margin, is an indication of robustness to plant uncertainty. Given a plant P and a stabilizing controller C, this margin is given by equation 2.24.

$$b_{P,C} = \left|\left| \begin{bmatrix} P \\ I \end{bmatrix} (1 - CP)^{-1} \begin{bmatrix} -C & I \end{bmatrix} \right|\right|_\infty^{-1} \tag{2.24}$$

Here, $b_{P,C} \in [0, 1]$, where higher stability margin indicates increased robustness to plant perturbations. A stability margin of 0 indicates internal instability. Strong robustness results are related to the ν-gap metric described in section 2.4.1 and the gap metric stability margin. That is, given a plant P and a stabilizing controller C, the controller will stabilize

all plants in the set $\mathcal{B}$, where $\mathcal{B}$ is given by equation 2.25 [28].

$$\mathcal{B} = \{P^* | b_{P,C} > \delta_v(P, P^*)\} \tag{2.25}$$

Hence, the gap metric stability margin can be used as a stability requirement for aircraft in icing condition. Given a nominal plant at a given icing level, P, and a stabilizing controller, C, the controller stabilizes the plant, $P^* \in \mathcal{B}$, for any icing level where this condition is true.

2.5 Gain-Scheduled Control

A gain-scheduled controller consists of several controllers, each designed for different operating points in the operational area. Then, a switch is used to select the appropriate controller given the system state. Here, it is vital to have a switching mechanism that does not introduce undesirable transients. Gain-scheduling allows the use of simple linear control methods to control non-linear systems where the process gain is changing considerably at different operating points [29]. In other words, this approach can be used when a single linear controller does not provide the desired performance and stability for all operating points. For this method to be feasible, the states/variables that change the operating point needs to be measurable.

Part II

Methodology

Chapter 3

Flight Control Analysis Toolbox

As previously mentioned, Flight Control Analysis Toolbox (FCAT) [18] is a software package in python made for simulating and analyzing flying rigid bodies. FCAT's architecture is based on the separation of concern (SoC) principle, where functionality is separated into independent building blocks. FCAT is configured with continuous integration pipeline, enforcing automation in building and testing. Figure 3.1 shows the program flow chart. The red blocks are configured from user input, the blue blocks are internal functions, and the green blocks are system output.

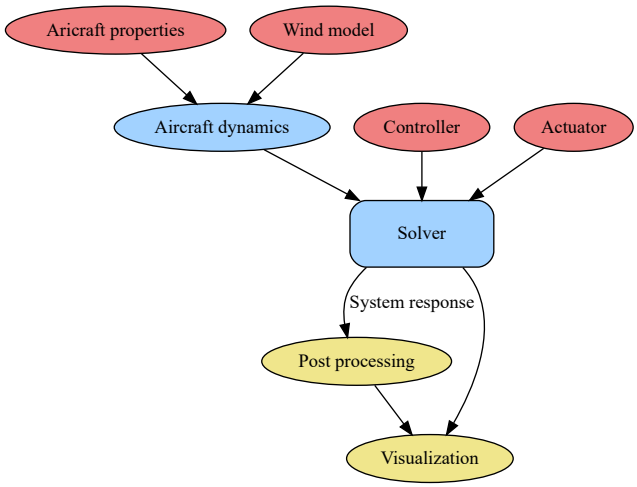

Figure 3.1: Software flow chart

Python Control Systems Library [30] is used to construct a simulation model. Figure 3.2

shows a block diagram of the final interconnected system, where each of the blocks is input/output system sub-classes. Here, r is the reference signal, u_c is the commanded control signal and u_a is the actual control signal. These input/output systems are built and connected based on the user inputs. Any of the blocks can easily be removed or replaced by more complicated algorithms. This design makes it easy to extend the application.

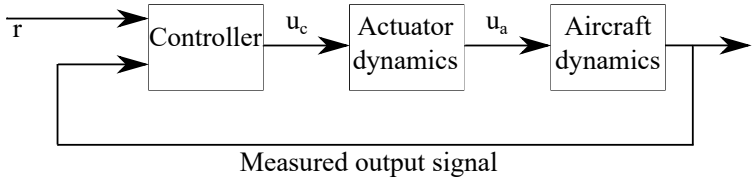

Figure 3.2: Simulation block diagram

Physical actuators have both static and dynamic limitations. The static constraints are handled by the controller block using minimum/maximum saturation on the control signals. The dynamic limitations are handled by having an actuator dynamics block. Here, it is implemented using a simple first order model as shown in equation 3.1.

$$\frac{u_a}{u_c} = \frac{\frac{1}{\tau}}{1 + \frac{1}{\tau}s} \tag{3.1}$$

Here, τ is the actuator time constant, given by the inverse of the rate limit.

The aircraft dynamics block is implemented as a non-linear input/output system and is realizing the twelve-state model from section 2.1. It is worth noticing that this model uses the Euler angles and not quaternions. The drawback here is the singularity problem that arises if the pitch-angle is $\frac{\pi}{2}$. The advantage is that one can use out of the box linearization tools to linearize the actual simulation model when performing system analysis. The aircraft dynamics block is built based on the FCAT classes AircraftProperties and WindModel as shown in figure 3.1.

AircraftProperties is implemented as an abstract class, which are collecting fluid mechanical coefficients needed to describe the dynamics of a rigid body in equation 2.8. AircraftProperties represent a rigid flying body where the control inputs are fixed. Thus, concrete implementations of this class should return the fluid mechanical coefficients when the control variables are given. This way, any rigid flying body can be implemented. This is very convenient when it comes to code testing of the aircraft dynamics block. In this regard, concrete implementations of a frictionless ball, a simple aircraft without aerodynamic forces and a simple aircraft without aerodynamic moments are implemented and tested against analytical solutions. The concrete implementation of the Skywalker X8 based on section 4 is implemented for later system analysis. An asymmetric extension of this model based on the principles in section 2.1.6 is also implemented.

The WindModel class is an abstract class that represents the general wind model. Two concrete implementations are made. Those are ConstantWind and DrydenGust. The latter is based on the description in section 2.2.

The solver block is simply an ordinary differential equation (ODE) solver that can be chosen appropriate to an ODE problem. The post-processing and visualization are separate output modules. At this point, the system input/output responses are analysed.

Chapter 4

Skywalker X8 Simulation Model

The UAV used for analysis in this thesis is Skywalker X8. This chapter describes how a complete simulation model for Skywalker X8 is obtained by using the theory from section 2.1.

4.1 Flying Wing

The skywalker X8 belongs to a class of aircraft called flying-wing. Figure 2.2 shows the shape of the aircraft. A flying wing aircraft has no rudder, and the remaining two aerodynamic control surfaces, namely ailerons and elevators, are combined into a pair of elevons. By denoting the left and right elevon deflection as δ_{el} and δ_{er} respectively, the mathematical conversion between elevon deflection to aileron-elevator deflections are given by equation 4.1 [5].

$$\begin{bmatrix} \delta_e \\ \delta_a \end{bmatrix} = \frac{1}{2} \begin{bmatrix} 1 & 1 \\ -1 & 1 \end{bmatrix} \begin{bmatrix} \delta_{er} \\ \delta_{el} \end{bmatrix} \tag{4.1}$$

Therefore, the mathematical model for forces and torques for flying wing aircraft can still be expressed in terms of standard aileron-elevator deflections notation as in equation 2.8.

4.2 Aerodynamic Functions

This subsection will present the structure of the simulation model and how the model is extended to include icing conditions.

4.2.1 General Aircraft Model without Ice

The aircraft lift force-, drag force-, side force-, pitching moment-, rolling moment- and yawing moment functions in equation 2.8 are generally non-linear equations of the system states. These functions can be simplified by acceptable accuracy using linear approxima-

tions [5]. The simplified functions using first-order Taylor series expansions are shown in equation 4.2.

$$\begin{bmatrix} C_D(\alpha,q,\delta_e) \\ C_Y(\beta,p,r,\delta_a) \\ C_L(\alpha,q,\delta_e) \\ C_{\mathrm{l}}(\beta,p,r,\delta_a) \\ C_{\mathrm{m}}(\alpha,q,\delta_e) \\ C_{\mathrm{n}}(\beta,p,r,\delta_a) \end{bmatrix} = \begin{bmatrix} C_D(\alpha) + \frac{c}{2V_a} C_{D_q} q + C_{D_{\delta_e}} \delta_e \\ C_Y(\beta) + \frac{b}{2V_a} C_{Y_p} p + \frac{b}{2V_a} C_{Y_r} r + C_{Y_{\delta_a}} \delta_a \\ C_L(\alpha) + \frac{c}{2V_a} C_{L_q} q + C_{L_{\delta_e}} \delta_e \\ C_{\mathrm{l}}(\beta) + \frac{b}{2V_a} C_{\mathrm{l}_p} p + \frac{b}{2V_a} C_{\mathrm{l}_q} q + C_{\mathrm{l}_{\delta_a}} \delta_a \\ C_{\mathrm{m}}(\alpha) + \frac{c}{2V_a} C_{\mathrm{m}_q} q + C_{\mathrm{m}_{\delta_e}} \delta_e \\ C_{\mathrm{n}}(\beta) + \frac{b}{2V_a} C_{\mathrm{n}_p} p + \frac{b}{2V_a} C_{\mathrm{n}_r} r + C_{\mathrm{n}_{\delta_a}} \delta_a \end{bmatrix} \tag{4.2}$$

Here, the partial derivative of a state is denoted with subtext. That is, C_{i_x} is the partial derivative of C_i with respect to x. $\frac{c}{2V_a}$ and $\frac{b}{2V_a}$ are standard factors used to keep the functions dimensionlessness. Another change made in 4.2 is δ_r is removed from the equation set. This is due to Skywalker X8 does not have a rudder, as addressed in section 4.1. Due to the non-linear nature of C_D, C_L and C_m in the angle of attack, α, and C_Y, C_l and C_n in the angle of sideslip, β, these coefficients are kept as a non-linear function to give more accuracy to the simulation model.

4.2.2 Icing Model

The extension of the aircraft model to include icing conditions is done based on the work in Winter *et al.* [31]. By denoting the icing level variable as $\zeta \in [0,1]$, describing the level of icing, where $\zeta = 0$ indicates no ice (referred to as clean) and $\zeta = 1$ indicates the worst-case level of ice (referred to as iced). Icing level $\zeta = 1$ correspond to the worst-case icing configuration, which is called mixed-ice and is a mixture of glaze ice and rime ice [3]. The model is extended to include icing effects by using linear interpolation between the clean and iced case for each coefficient in the Taylor series expansion in equation 4.2. This includes all the partial derivatives and the non-linear coefficients depending on the angle of sideslip or angle of attack. The general coefficient C_k given as a function of the icing level ζ is shown in equation 4.3.

$$C_k(\zeta) = C_{k,0} + \zeta(C_{k,1} - C_{k,0}) \tag{4.3}$$

Here, $C_{k,0}$ is the coefficient value for the clean case and $C_{k,1}$ is the value for the iced case.

4.2.3 Physical Measures

The Skywalker X8 physical measures are given in appendix B.2. The moments- and products of inertia are shown in table B.3. These values are based on experimental data from Gryte [32].

In the asymmetric model described in section 2.1.6, the point of attack for the aerodynamic forces acting on the Skywalker X8 must be specified. It is not possible to state these exact points based on the data available. Hence, the points used in later simulations are based on qualified guessing. Note that the purpose of simulating an asymmetric icing condition in this thesis is to capture the asymmetric effects rather than giving an exact reproduction of a real system.

The UAV is shown in figure 2.2. For simplicity, all points of attacks are assumed to lie on the $\pm$y - axis. This assumption is reasonable, because the largest asymmetric moment contributions, which is from drag force to yaw moment and from lift force to roll moment are retained. Another assumption made is that icing level does not effect the points of attacks y-coordinate. By combining these assumptions, the relation between distance vector from the centre of mass to the left wing center of pressure, $\mathbf{l}_i$, and right-wing center of pressure, $\mathbf{r}_i$, for $i \in \{D, S, L\}$ is given in equation 4.4.

$$\mathbf{l}_i = -\mathbf{r}_i \implies \begin{bmatrix} 0 \\ y_{i,l} \\ 0 \end{bmatrix} = - \begin{bmatrix} 0 \\ y_{i,r} \\ 0 \end{bmatrix} \tag{4.4}$$

Where $y_{i,l}$ and $y_{i,r}$ is the y coordinate of the centre of pressure for left -and right-wing in body frame.

The wingspan is 2.1 meters (m), which means that the distance from the centre of mass to the tip of one wing is 1.05 m. By intuition, the fuselage will give a larger contribution to the drag force than the wings. Hence the point of attack for the aircraft drag force will have to lie somewhere between the centre of mass and the middle of the wing. $y_{D,r}$ is therefore chosen to be 0.25 m. The lift force is intuitively largest at the part of the wing closest to the fuselage and decreases along the wing. Hence $y_{L,r}$ is chosen to be 0.4 m. For the side force, the main contributions are from the fuselage and the winglets on the tip of the wing. $y_{S,r}$ is chosen to be 0.2 m. The side force is typically smaller in magnitude than the lift and drag forces. In addition, having the point of attack on the $\pm$y - axis will make the asymmetric moment contribution from the side force small.

4.2.4 Aerodynamic Coefficient Values

The model coefficients in equation 4.2 for this specific UAV are found through wind tunnel experiments in the aerodynamic modelling work done by Gryte *et al.* [8]. The icing level extension is based on the analysis of the results from Computational Fluid Dynamics (CFD) simulations done by Winter [3]. As emphasized by Winter *et al.* in [31], the atmospheric icing will primarily affect the leading edge of the aircraft. Hence, the control derivatives, namely $C_{D_{\delta_e}}$, $C_{Y_{\delta_a}}$, $C_{L_{\delta_e}}$, $C_{\mathrm{l}_{\delta_a}}$, $C_{\mathrm{m}_{\delta_e}}$ and $C_{\mathrm{n}_{\delta_a}}$, are assumed to be independent of icing level. The aerodynamic coefficient values used in later simulations are given in table B.1 in appendix B.

The aerodynamic functions of angle of attack (AOA) and angle of sideslip (AOS) is shown in figure 4.1a and 4.1b respectively. In 4.1a, AOS$\approx 0.00\,\mathrm{deg}$ is kept constant while AOA sweeps from -5 to 16 degrees. In 4.1b. AOA$\approx 2.11\,\mathrm{deg}$ is kept constant while AOS sweeps from -10 to 10. The green curves are showing icing level $\zeta = 1$, the blue curves are showing icing level $\zeta = 0$ and the red curves are showing the asymmetric case with icing levels $\zeta = 0$ and $\zeta = 1$ on the left- and right-wing respectively. Figure 4.1 illustrates the general effects of icing. It is clear that the drag force is increased, and the lift force is decreased with icing. These effects increase with the angle of attack. It is also worth noticing that the roll-off in the lift coefficient starts at a lower angle of attack when ice is present. As a consequence, the angle where the lift coefficient exceeds the value which creates maximum lift, also known as stall angle, is lower for the iced case. Figure 4.1

illustrates that the effect of icing on the lift coefficient at low AOA is small. Since the largest effects of icing conditions are on the drag -and lift force in the symmetric case, it is clear that the effects of symmetric icing are primarily in the longitudinal direction.

The effects of asymmetric icing are also illustrated in figure 4.1. For all force functions, the result of asymmetry is simply the average of the icing levels on each wing. Hence, the asymmetric curves for the force function are here equivalent to the symmetric case with icing level $\zeta = 0.5$. Due to the selected points of attacks in section 4.2.3, there are no additional contributions to the pitching moment function from asymmetry. Hence this function is simply the average of the icing levels on left and right-wing as well.

The asymmetric effects for the lateral aerodynamic functions are more significant. As illustrated in 4.1a, these functions are very dependant on the drag and lift forces. This lead to increased cross-coupling between the lateral and longitudinal dynamics.

4.3 System Analysis

This section describes the methods used for linear analysis, including dynamic mode analysis on the effects of icing conditions to determine static stability properties. The methods presented in this section are also used in the linear controller synthesis.

4.3.1 Linearization

Analyzing the behaviour of a control process and developing linear controllers is done using linear approximation at a given operating point. The Python Control Systems Library function [30] **linearize** is used to linearize the dynamic system. In general, the linearized system can be written as in equation 4.5.

$$\Delta\dot{\mathbf{x}} = \frac{df}{d\mathbf{x}}\Delta\mathbf{x} + \frac{df}{d\mathbf{u}}\Delta\mathbf{u} \tag{4.5}$$

Here, $\frac{df}{d\mathbf{x}}$ and $\frac{df}{d\mathbf{u}}$ are the jacobian matrices of $\mathbf{f}$ with respect to the state vector $\mathbf{x}$ and control input vector $\mathbf{u}$ respectively. $\mathbf{f}$ for a system with n states is defined as in equation 4.6.

$$\mathbf{f} = \begin{bmatrix} \dot{x_1} \\ \dot{x_2} \\ \vdots \\ \dot{x_n} \end{bmatrix} = \begin{bmatrix} f_1 \\ f_2 \\ \vdots \\ f_n \end{bmatrix} \tag{4.6}$$

The **linearize** function uses a finite difference method to calculate the linearized system. This method is summarized by equiation 4.7.

$$\frac{df_i}{\partial x_j} = \frac{f_i(\mathbf{x} + \mathbf{e}_j\Delta x) - f(\mathbf{x})}{\Delta x} \tag{4.7}$$

Here, e_j is a vector of the same length as $\mathbf{x}$, where the jth element is 1, and all other elements are 0. Δx is generally a small value. Here the default value of 10^{-6} is used.

4.3.2 Trim Condition

It is common to use a trim point as the operating point when studying the aircraft behaviour at level-fight. Mathematically, trim conditions can be found by solving a set of non-linear algebraic equations. This is explained in detail in Beard and McLain [5]. In this thesis, the Python Control Systems Library [30] function **find_eqpt** is used to calculate the trim conditions. This function starts from a given initial point and then uses a root-finding algorithm to find the nearest trim point of the dynamical system.

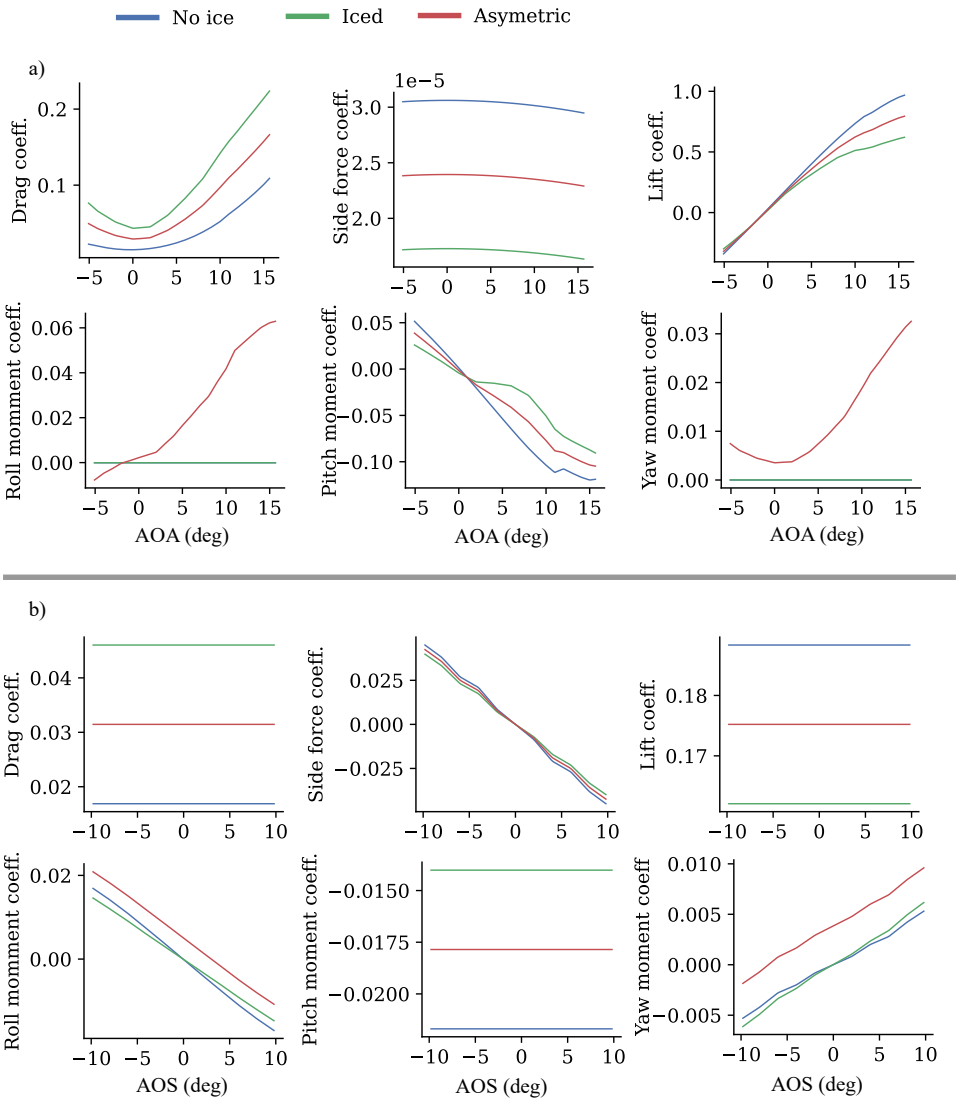

Figure 4.1: Aerodynamic Functions

Chapter 5

Controllers

This chapter will describe the tuning process of the inner loop controllers. The task of the low-level inner loop control system is to stabilize the body-frame states using measurements and actuators. In other words, the inner loop keeps the aircraft flying, where the tasks of the higher level outer loop control is to implement guidance. The inner loop control objective is to stabilize the dynamics. That is, tracking desired roll, pitch and airspeed.

5.1 Systematic loop-shaping design procedure

The control objective is to have controllers that fulfil closed-loop requirements regarding performance, robustness and stability. In this thesis, a robust controller is obtained by tuning weighting filters using the output feedback H_∞ method as described in section 2.3. This section will describe the loop-shaping procedure. As mentioned in the introduction, this tuning method is based on the same ideas that is presented in the pre-master project [1]. However, this is a different dynamic system. In addition, the tuning method from the pre-master project [1] has also been improved to get even better disturbance rejection.

5.1.1 Closed-loop Requirements

This particular control problem has several important factors to take into account. It is desirable that the controller stabilizes a set of perturbed plants for different levels of ice. A stability requirement for guaranteed stability for a set of perturbed plants can be established using the theory in section 2.4. By having a nominal plant P_0 at a icing level $\zeta \in [0, 1]$, worst-case iced plant P_{ice} at icing level $\zeta = 1$ and plant with no ice P_{clean}, the stability requirement can be stated as in equation 5.1.

$$b_{P_0,C} > \max(\delta_\nu(P_0, P_{\text{ice}}), \delta_\nu(P_0, P_{\text{clean}})) \tag{5.1}$$

Where $b_{P_0,C}$ is the gap metric stability margin and δ_ν is the ν-gap metric. Furthermore, assuming that the ν-gap distance between two plants is increasing when the difference in icing level is increasing, the stability criterion implies that the controller stabilizes plants for all icing levels. The assumption is mathematically shown in equation 5.2.

$$\delta_\nu(P(\zeta_0), P(\zeta_1)) < \delta_\nu(P(\zeta_0), P(\zeta_2)) \text{ for } \begin{cases} \zeta_0 < \zeta_1 < \zeta_2 \\ \zeta_2 < \zeta_1 < \zeta_0 \end{cases} \tag{5.2}$$

This assumption is reasonable since the icing model is found by linear interpolation between the iced and clean case.

As seen while modelling the Skywalker X8, any model of a physical system will never be a true representation of that system. Hence, requirements for general margins from control theory, such as gain-, phase- and stability margins, should also be of sufficient magnitude for robustness to unmodeled dynamics. According to Astrom and Murray [29], reasonable closed-loop robustness requirements are;

- Minimum phase margin $\phi_m = 30°$
- Minimum gain margin $g_m = 2$
- Minimum stability margin $s_m = 0.5 - 0.8$

These margins are used as lower thresholds in this thesis.

The performance can be measured in terms of maximum closed-loop overshoot and settling time when the system is subject to a step in the reference signal. Acceptable values of settling time and overshoot are dependant on the controlled variable. Hence, these specifications will be mentioned in each specific simulation. Since the controller goal is to have satisfactory performance for different levels of ice, there will be a trade-off between performances for different plants.

5.1.2 Weighting Filters

The weighting filters should, in general, be selected to be of minimum order in order to avoid adding unnecessary complexity to the controller [6]. Higher-order weighting filters results in higher-order controllers. The general loop-shaping principles on the desired shapes of complementary sensitivity- and sensitivity functions described in section 2.3.2 is the foundation of the tuning process. These principles set the general shapes of the filters, as seen in equation 5.3.

$$W_S = \frac{s/M + 1}{s + \omega_0 A} \tag{5.3a}$$

$$W_C = \text{Constant} \tag{5.3b}$$

$$W_T = \frac{s + \omega_0/M}{As + \omega_0} \tag{5.3c}$$

Here, ω_0 is the desired controller bandwidth, M is limiting the maximum sensitivity peak and A limits the low-frequency gains. Control activity is limited by the $|W_C|^{-1}$. By choosing W_C as a constant, all control activity is penalized equally at all frequencies. Too low penalty on the control signal may lead to oscillatory responses. Too high penalty on the control signal may limit the closed-loop bandwidth, which in turn gives worse reference tracking. As mentioned in chapter 2.3.2, W_T are usually formed to get sufficient noise attenuation and robustness to uncertain high-frequency dynamics. High-frequency noise is not implemented in this model. Hence, W_T is chosen as a first-order high pass filter with the same crossover frequency as W_S, as shown in equation 5.3. However, it is important to keep in mind that unrealistic high bandwidths will give poor results for real systems.

There are cases where it is necessary to use higher-order filters. For instance, one can increase the controller integral action by increasing the order of the tuning filters. The general equation for a second-order sensitivity filter is given by equation 5.4.

$$W_S = \frac{(s/M^{\frac{1}{2}} + \omega_0)^2}{(s + \omega_0 A^{\frac{1}{2}})^2} \tag{5.4}$$

By choosing $M = 2$, $A = 10^{-5}$ and $\omega_0 = 6.8$, the frequency response for the first and second order sensitivity filters are shown in figure 5.1.

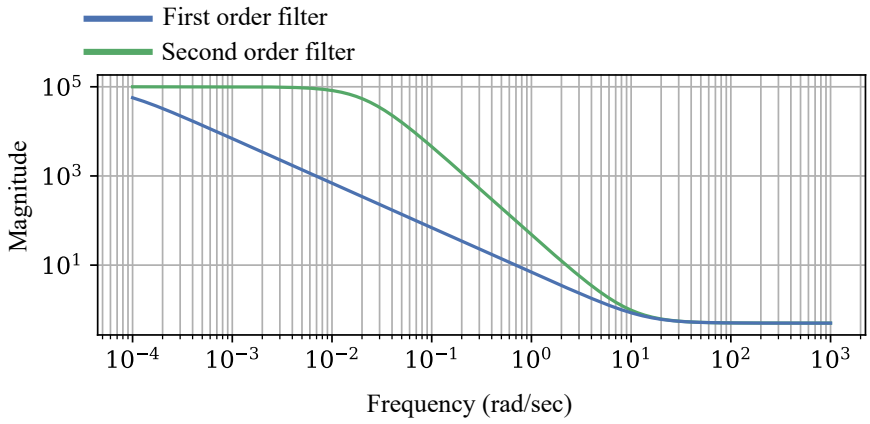

Figure 5.1: Frequency plot of first- and second order filter

This will generally give better disturbance rejection. However, it tends to degrade the controller performance in the form of increasing the step-overshoot. Figure 5.2 illustrates the effect of lacking integral action. This shows the time responses using the sensitivity filters in 5.1. Figures 5.1b and 5.1d shows the time responses for a step in input and a constant disturbance at $t = 5$ seconds, respectively. Figure 5.1a shows the control signal for a step in reference, and figure 5.1c shows the control signal for the constant disturbance case. The disturbance response is very good using a second-order filter, whereas the tracking response has a quite large overshoot. For the first-order filter, the step response gives no overshoot. However, the disturbance response is very poor because the integral action using the first-order filter is low. Hence, the response will move slowly towards the reference

value when subjected to disturbance.

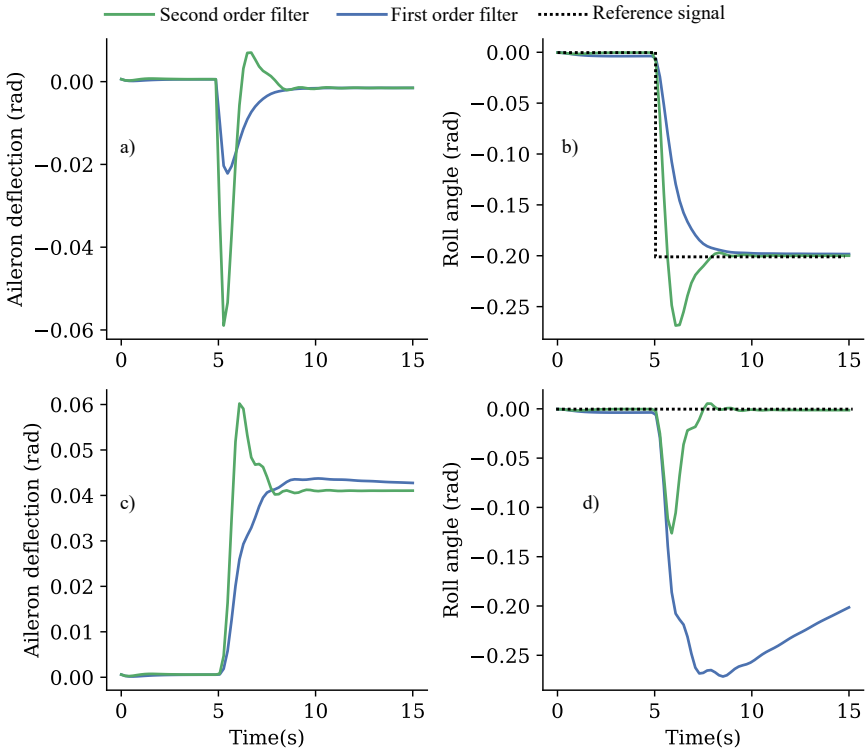

Figure 5.2: *a*) and *b*) time response of a step in reference. *c*) and *d*) time response constant disturbance.

5.1.3 Controller Tuning Process

The loop-shaping tuning process can be summarized in the following steps.

- Finding the icing level for the nominal plant that minimizes the maximum ν-gap distance to the extreme cases. The plant at this icing level is used for the controller synthesis. In other words, the nominal plant is chosen to be at the midpoint of the worst-case plants. This choice will give the most relaxed stability requirement, as the right term in equation 5.1 will be minimized. This choice is also performance-related. Typically, increasing and decreasing the icing level will give opposite closed-loop performance effects. Either give a more rapid response with a higher overshoot or a slower response and a lower overshoot. Hence, choosing a midpoint nominal plant will minimize the qualitative differences in closed-loop responses from nominal to worst-case plants.

- Select the desired range of sufficient bandwidth frequencies. Here, the elements of noise attenuation and fundamental limitations like right half plane zeros and time

delays should be taken into account when choosing the upper threshold. The lower threshold should be chosen based on minimum performance requirements related to reference tracking.

- Finding filter parameter values in equation 5.3 based on an iterative process. A is chosen such that the low-frequency disturbance rejection is sufficient. For SISO systems, the stability margin is given by the maximum peak of the sensitivity transfer function. Hence M is chosen based on the stability margin requirement. ω_0 is chosen to be the minimum frequency in the frequency range chosen in step 2. Then W_C is adjusted such that the system response is non-oscillatory. The robustness-, stability- and performance requirements are then checked for both the worst-case and nominal plants. As long as all the requirements are met, ω_0 is increased, and this step is repeated. The idea is to get as high as possible bandwidth within the target frequency range to achieve good performance while robustness and stability requirements are met.
- If the final controller does not have sufficient disturbance rejection, increase the filter order on the sensitivity function as shown in equation 5.4, and repeat the last step.

5.2 Longitudinal and Lateral Decoupling

The controller designs are based on separating the longitudinal and lateral dynamics and synthesizing in-dependant control systems. This is a common method for linear aircraft control designs, and it is used by Beard and McLain [5] and Lavretsky and Wise [6]. This type of decoupling is only suitable for gentle manoeuvring and not in cases where there is a high degree of lateral-longitudinal cross-coupling nor for aggressive manoeuvres. Even if Skywalker X8 is a flying wing, and the aileron and elevator are combined into a pair of elevons, this separation is still doable using the relationship in equation 4.1. Note that the simulation model itself has been simplified to be separated into the longitudinal -and lateral direction (see section 2.1.3). Hence, these controllers may be more vulnerable to aggressive manoeuvres in real life than in this simulator.

5.2.1 Longitudinal Control

The inner-loop longitudinal controller sets the desired elevator deflection based on the commanded pitch angle and desired throttle based on commanded airspeed. A longitudinal state vector can be extracted from the linearized system in equation 4.5. The longitudinal state vector and inputs are defined as in equation 5.5

$$\mathbf{x}_{\text{lon}} = \begin{bmatrix} u \\ w \\ q \\ \theta \end{bmatrix} \tag{5.5a}$$

$$\mathbf{u}_{\text{lon}} = \begin{bmatrix} \delta_e \\ \delta_t \end{bmatrix} \tag{5.5b}$$

The longitudinal state space model can then be written as in equation 5.6.

$$\Delta\dot{\mathbf{x}}_{\text{lon}} = \frac{df_{\text{lon}}}{d\mathbf{x}_{\text{lon}}}\Delta\mathbf{x}_{\text{lon}} + \frac{df_{\text{lon}}}{d\mathbf{u}_{\text{lon}}}\Delta\mathbf{u}_{\text{lon}} \tag{5.6}$$

The longitudinal open-loop dynamics includes the short period modes and the phugoid modes. The airspeed and pitch angle are two coupled states that are controlled by two control variables. Thrust, δ_t, is the primary airspeed control variable and elevator deflection, δ_e, is the primary pitch control variable. This control problem is approached by having two SISO controllers and introduce a state-machine with modes that are used to decide how commanded thrust and commanded pitch are calculated. Typical state-machine modes of operation are Descend mode, Climb mode and Level flight mode. This approach is described in Beard and McLain [5]. As previously mentioned, this thesis handles inner-loop control, and how the desired pitch is calculated is not in this scope. Generally, when controlling two coupled states with decoupled controllers, states may be driven away from their equilibrium point. For instance, if airspeed is being kept constant by the throttle controller, the altitude responds rapidly to even small changes in aircraft pitch. The controller from commanded pitch, θ_c, to elevator deflection, δ_e, is an H_∞ - controller. The airspeed controller is implemented as a simple PI controller.

Airspeed Control

As seen in section 4.2.4, one of the main effects of icing is increased drag. This means that the throttle needed to maintain the airspeed is increased. Consequently, this will also lower the maximum airspeed possible to achieve for the UAV. For considering in-flight airspeed control well below the maximum achievable airspeed, a single PI airspeed controller with an anti-windup scheme is found and used for all cases in the simulation. The output of the airspeed controller is given by equation 5.7.

$$\delta_t = \tilde{\delta}_t + (K_p + \frac{K_i}{s})(V_a^c - V_a) \tag{5.7}$$

Where $\tilde{\delta}_t$ is the calculated trim-value, and K_p and K_i are tuning parameters. Here, it is important to not have too aggressive gains since this may lead the throttle to cut and surge. Therefore, the controller is tuned for an acceptable error, and then the integral term closes the error gap. The tuning parameters used in this thesis is based on trial-error tuning, where $k_p = 0.068$ and $k_i = 0.057$ is found suitable. Figure 5.3 shows the step-response in airspeed for the iced and clean case. Here, it is clear that the required throttle to maintain airspeed is higher in icing conditions. This is a direct result of the increased drag force.

Pitch Control

The iterative tuning process described in section 5.1.3, is performed for the pitch-controller. Here, γ^*_{lon} is the achieved controller performance value described in section 2.3.3. For the performance requirements, the acceptable overshoot is chosen to be 10 %. The frequency range is chosen to be $\omega_0 \in [1, 13.8]$. The maximum frequency is chosen based on Lavretsky and Wise [6]. Note that even the aircraft in Lavretsky and Wise [6] differs from the Skywalker X8, the noise attenuation requirements are comparable. The pitch controller

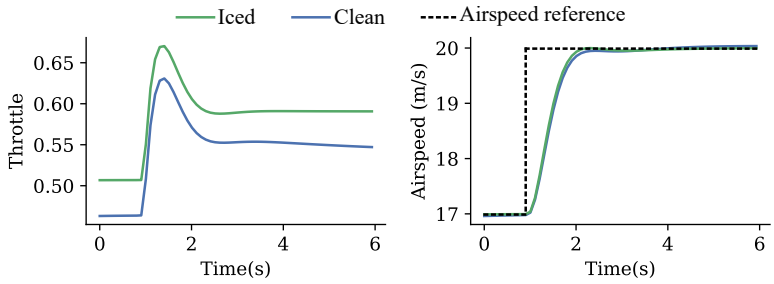

Figure 5.3: Airspeed step response for iced and clean case.

used here are using first order tuning filters. As previously discussed, this gives more precise reference tracking in terms of lower overshoots to changes in input. On the other hand, this may lead to low integral action, which again can lead to steady state errors when subject to low frequency disturbances. As seen, symmetric icing does primarily affect the longitudinal dynamics, and icing can be classified as a low frequency disturbance. This mean that steady state error in pitch is expected when the UAV is subject to icing conditions. The main argumentation for still using first order filters for longitudinal direction is that as long as this steady state error is small enough and the disturbance response is not too slow, this error can be corrected for by an higher-level outer loop controller. The robust pitch controller parameters are summarized in table 5.1. The icing level for nominal plant uses for the pitch controller synthesis was found to be $\zeta = 0.3$. This lead to an ν-gap of less than 0.31 to the worst case plants.

Table 5.1: Longitudinal Robust Controller Summary

Performance parameter	Value
γ^*_{lon}	1.9617
Filter parameter	**Value**
ω_0	6.2 rad/s
M	2
A	0.001
W_C	1

A similar approach is made for the gain-scheduled case. Here, the icing-level resolution is chosen to be 0.2. I.e. a controller is selected if the icing level is within ± 0.1 of its nominal plant. The icing-levels chosen is then $\zeta_{\text{nominal}} = \{0.1, 0.3, 0.5, 0.7, 0.9\}$. By using this tuning approach for gain-scheduling, the stability criterion is significantly relax, since the worst case icing-levels are now defined $\zeta_{\text{nominal}} \pm 0.1$. The gain scheduled controllers are summarized in table 5.2. It is worth noticing that it is the frequency range that terminates the iterative process for all gain-scheduled pitch controllers. The gain-scheduled controller is only implemented with a simple switch, meaning when the icing level changes from the area of one controller to another, the controller is switched instantaneously. As briefly mentioned in chapter 2, this may lead to undesired transients. Hence, the gain-scheduled controller is used to investigate the performance improvement within the icing-area of one

controller, rather than scenarios related to de-icing and ice accretion.

Table 5.2: Longitudinal gain scheduled controllers with icing level value ζ

Performance parameter	$\zeta = 0.1$	$\zeta = 0.3$	$\zeta = 0.5$	$\zeta = 0.7$	$\zeta = 0.9$
γ^*_{lat}	3.6298	3.5165	3.3971	3.2827	3.1956
Filter parameters					
ω_b (rad/s)	13.8	13.8	13.8	13.8	13.8
M	2	2	2	2	2
A	0.001	0.001	0.001	0.001	0.001
W_C	1.0	1.0	1.0	1.0	1.0

5.2.2 Lateral Control

The lateral controller sets the desired aileron deflection based on the commanded roll angle. The lateral state vector and inputs are defined as in equation 5.8.

$$\mathbf{x}_{\text{lat}} = \begin{bmatrix} v \\ p \\ r \\ \phi \end{bmatrix} \tag{5.8a}$$

$$u_{\text{lat}} = \delta_a \tag{5.8b}$$

Similarly as for the longitudinal case, the lateral state equations are extracted from the linearized model in equation 4.5. This gives the following lateral state space equations;

$$\Delta\dot{\mathbf{x}}_{\text{lat}} = \frac{df_{\text{lat}}}{d\mathbf{x}_{\text{lat}}}\Delta\mathbf{x}_{\text{lat}} + \frac{df_{\text{lat}}}{d\mathbf{u}_{\text{lat}}}\Delta\mathbf{u}_{\text{lat}} \tag{5.9}$$

.

The lateral open-loop dynamics of the UAV includes the roll rate damping mode, a spiral mode and the dutch roll mode. The implementation of the lateral controller will be described in greater detail in section 5.1.

Roll Control

As seen in section 2.1.6, the lateral dynamics is sensitive to asymmetric disturbances. Since one of the main objectives of the controllers in this thesis is disturbance rejection, and coping with asymmetric conditions, the lateral controller is using a second-order sensitivity filter to increase the controller integral action. The steady state errors for the lateral controller in the asymmetric case were too large for the controller using first order tuning filter. The same iterative tuning process is performed for the lateral controller. Here, the performance requirements for overshoot is chosen to be 30 %. It is important to notice

that high integral action may lead to oscillatory responses. One way to avoid this type of unwanted behaviour is to tighten the closed-loop robustness requirements. Here, the stability margin $s_m = 0.7$ is used. This is still within the area given by Astrom and Murray [29]. The frequency range is chosen to be $\omega_0 \in [1.0, 10.0]$. The lateral controller parameters are shown in table 5.3. The icing level for nominal plant uses for the lateral controller synthesis was found to be $\zeta = 0.3$. This lead to an ν-gap of less than 0.1 to the worst case plants. This gap is considerably lower than in the longitudinal case, which is a consequence of symmetric icing conditions having its primarily effects on the longitudinal direction.

Table 5.3: Lateral robust controller summary

Performance parameter	Value
γ^*_{lon}	1.9199
Filter parameter	Value
ω_0	2.1 rad/s
M	2
A	0.0002
W_C	1

The same approach is repeated for the gain-scheduled controller. Here, the icing-level resolution is chosen to be the same as for the longitudinal case, 0.2. I.e. a controller is selected of the icing level is within ± 0.1 if its nominal plant. The icing-levels chosen is then $\zeta_{\text{nominal}} = \{0.1, 0.3, 0.5, 0.7, 0.9\}$. The lateral gain scheduled controllers are summarized in table 5.4. The switching mechanism for the lateral controller is similar to the one described for the pitch controller.

Table 5.4: Lateral gain scheduled controllers with icing level value ζ

Performance parameter	$\zeta = 0.1$	$\zeta = 0.3$	$\zeta = 0.5$	$\zeta = 0.7$	$\zeta = 0.9$
γ^*_{lat}	2.1699	2.2860	2.3216	2.2860	2.3128
Filter parameters					
ω_b (rad/s)	2.9	3.2	3.3	3.2	3.2
M	2	2	2	2	2
A	0.002	0.002	0.002	0.002	0.002
W_C	1.0	1.0	1.0	1.0	1.0

Chapter 6

Simulation Cases

This chapter presents the simulation cases used to evaluate the the controllers from chapter 5.

6.1 Controller Performance Tests

The controller performance tests are the tests that compare the single robust- and gain-scheduled controller performances. These tests are separated into two test runs to evaluate the longitudinal and lateral controllers. Here, it is especially roll and pitch controllers that are of interest, while the airspeed controller is only used for keeping the desired airspeed during the test runs. The manoeuvring capability is tested from a pre-defined sequence of commanded pitch angles in the longitudinal case and roll angles in the lateral case. These are all tested for icing levels $\zeta = \{0, 0.3, 1.0\}$. These levels are referred to as "clean", "some ice", and "iced". Two types of inputs are considered in these tests, namely ramp and step inputs of different magnitudes. These inputs are used to get the basic flight manoeuvres as climb, turn and descents.

The longitudinal test run is chosen to illustrate how the UAV controller handles basic flight manoeuvres climb and level-flight. By defining high pitch angle as $\theta = 20°$, medium pitch angle as $\theta = 10°$ and low pitch angle as $\theta = 0°$, the longitudinal test run is defined by the following sequence;

- Initial value at low pitch angle.
- Input ramp to high pitch angle with the slow rate (2°/sec), followed by constant input angle for 10 seconds.
- Input ramp back to low pitch angle with the slow rate (2°/sec), followed by constant input angle for 10 seconds.

- Input ramp to medium pitch angle with the fast rate (10°/sec), followed by constant input angle for 10 seconds.
- Input ramp to low pitch angle with the fast rate (10°/sec), followed by constant input angle for 10 seconds
- Step input to medium pitch angle, followed by constant input for 15 seconds.
- Consecutive input steps between low and medium pitch angles, with constant input angle for 2 seconds in between each step.

The lateral test run is chosen to illustrate how the UAV controller handles the basic flight manoeuvres turning and level-flight. By defining high roll angles as $\phi = \pm 40^\circ$, medium roll angles as $\phi = \pm 20^\circ$ and low roll angle to $\phi = 0^\circ$, the lateral test run given by the following sequence;

- Initial value at low roll angle.
- Input ramp to high positive roll angle with the slow rate (4°/sec), followed by constant input angle for 10 seconds.
- Input ramp to negative high roll angle with the fast rate (10°/sec), followed by constant input angle for 10 seconds.
- Input step to low roll angle, followed by constant input angle for 10 seconds.
- Input step to medium positive roll, followed by constant input angle for 15 sec.
- Consecutive input steps between negative medium roll angle and positive medium roll angle followed constant input angle for 2 seconds between each step.

6.2 Wind Conditions

A short performance test is simulated to verify the controllers' ability to track references in life-like wind conditions. Compensation for constant winds is commonly handled within the higher-level guidance controller rather than in the low level stabilizing inner-loop controllers. Therefore, this simulation is only looking at the wind gusts using the Dryden gust model from section 2.2. The simulation sequence used in wind conditions is;

- Initial value at low pitch and roll angles.
- Step input to medium pitch angle, followed by constant input for 10 seconds.
- Step input to low pitch angle and a simultaneous step input to positive medium roll angle, followed by constant input for 10 seconds.
- Step input to negative medium roll angle, followed by constant input for 10 seconds.

This input sequence is simulated with Dryden wind gusts of moderate intensity.

6.3 Icing Conditions

As briefly mentioned in the discussion, there are several aspects to icing conditions. Two icing test runs are simulated. The first test run is illustrating the effects of instantaneous de-icing, and simulation results are compared for different airspeeds.

- Commanded pitch, airspeed and roll are constant at trim conditions.
- Initial icing vale $\zeta = 1$.
- Sudden symmetric ice removal from $\zeta = 1$ to $\zeta = 0$ after 3 seconds.
- Sudden symmetric change in icing level to $\zeta = 1$ after 10 seconds.
- Piecewise asymmetric ice removal after 20 seconds. I.e. the rate at which ice is removed differs from left to right-wing. This simulates that ice flakes are suddenly falling of during ice removal. Here the icing on the left wing is $\zeta_{\text{left}} = 0$ and icing level on the right-wing is $\zeta_{\text{right}} = 0.5$ for 10 seconds, followed by the right-wing icing goes to $\zeta_{\text{right}} = 0.0$.

The second test run is looking at the scenario with a defect de-icing system on one of the wing;

- Commanded pitch, airspeed and roll are initially constant at trim conditions. Here, the airspeed is 21.4 m/s, the pitch angle is 2.4 degrees, and the roll angle is 0.0 degrees.
- Initial icing level $\zeta = 1$ on both wings.
- Initial step input to medium pitch angle (10 degrees), followed by constant pitch input for 10 seconds.
- Sudden asymmetric ice removal from $\zeta_{\text{left}} = 1$ to $\zeta_{\text{left}} = 0$ on the left wing after 3 seconds.
- Step input to low pitch angle (0 degrees), followed by constant input for 10 seconds.
- Step input to positive medium roll angle (20 degrees), followed by constant input for 10 seconds.
- Step input to low roll angle (0 degrees), followed by constant input for 10 seconds.

Part III

Results, Discussion and Conclusion

Chapter 7

Results

This chapter presents the results of the system analysis. The results include a section on how icing affects the dynamic modes of the Skywalker X8, as well as performance results using the controller design from chapter 5.

7.1 Dynamic Modes Analysis

When comparing icing-induced changes of the dynamic system to the basic clean case UAV, it is suitable to analyze the characteristics of the dynamic modes. By linearizing the non-linear aircraft dynamics at a given operating point, the eigenvalues can be found and used to determine the aircraft stability properties at this operating condition. This analysis is performed at trim points for low ($\alpha \approx 2.14\,\mathrm{deg}$) and high ($\alpha \approx 7.5\,\mathrm{deg}$) angles of attack. The airspeed is approximately 21 m/s for the low angle of attack and 13 m/s for the high angle of attack. As previously mentioned, the longitudinal dynamic modes consist of the short period -and phugoid modes and the lateral dynamic modes consist of rolling-, spiral -and dutch roll modes. Figures 7.1a and 7.1b shows how the lateral and longitudinal eigenvalues are affected at the trim point for a low angle of attack. Here, the filled circle denotes the eigenvalue in the clean case, and the cross denotes the eigenvalue in the iced case. The line shows the intermediate eigenvalues with a measurement resolution of 0.1.

The qualitative development of the eigenvalues as a function of ice is similar in the case of high and low angles of attacks. That is, the spiral mode moves from the left half-plane to the right half-plane, the other negative non-complex eigenvalues stays negative non-complex, and the negative complex-eigenvalues stays negative complex for all levels of ice at both low and high angles of attack. The longitudinal eigenvalues for the clean and

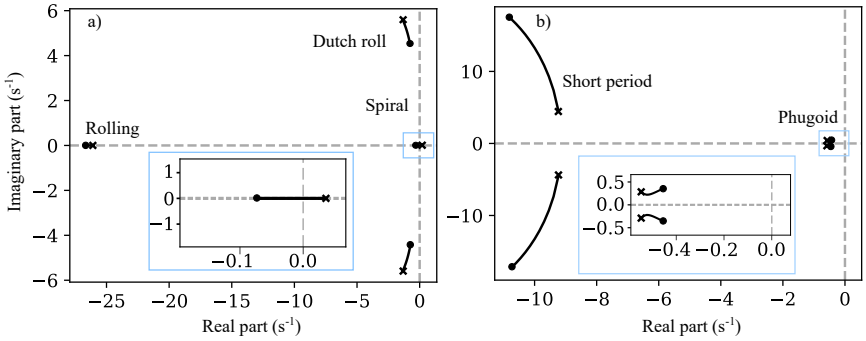

Figure 7.1: *a)*: the lateral dynamic modes in icing conditions. *b)*: longitudinal dynamic modes in icing conditions

iced case at high and low angles of attack are given by equation 7.1.

$$\begin{aligned} \mathrm{EV}_{\mathrm{lon}}(\alpha \approx 7.52^\circ, \text{iced}) &= \begin{cases} -5.482 \pm 8.043i \\ -0.364 \pm 0.672i \end{cases} \\ \mathrm{EV}_{\mathrm{lon}}(\alpha \approx 7.45^\circ, \text{clean}) &= \begin{cases} -5.892 \pm 9.645i \\ -0.255 \pm 0.483i \end{cases} \end{aligned} \tag{7.1a}$$

$$\begin{aligned} \mathrm{EV}_{\mathrm{lon}}(\alpha \approx 2.14^\circ, \text{iced}) &= \begin{cases} -9.235 \pm 4.565i \\ -0.544 \pm 0.277i \end{cases} \\ \mathrm{EV}_{\mathrm{lon}}(\alpha \approx 2.14^\circ, \text{clean}) &= \begin{cases} -10.745 \pm 17.245i \\ -0.459 \pm 0.345i \end{cases} \end{aligned} \tag{7.1b}$$

The largest change here is that for the low angle of attacks, the short period mode is considerably less damped in the clean case than in the iced case. The same effect on a much lower scale can be seen for high angles of attack. The phugoid mode in the iced case moves away further into the left half-plane from the clean case for both high and low angle of attacks. The phugoid damping ratio is increased with both an increase in angle of attack and ice. This may be explained by fact that the phugoid mode is dependant on the drag-to-lift ratio [13]. This ratio is generally changed in icing conditions, primarily due to the significant drag increase. Due to different arispeeds, it is also changed for trim conditions at different angles of attack.

The lateral eigenvalues for the clean and iced case at high and low angles of attack are given by equations 7.2. In the iced case, the spiral mode moves from the left to the right half-plane. In other words, icing destabilizes the spiral mode. Due to the spiral mode giving rise to very slow dynamic behaviour, it is not too critical to handling. Other than this, the effects of icing are quite small for the lateral dynamics. The Dutch roll mode becomes more damped. This can be attributed to the increased drag during icing conditions, which

in turn leads to increased local drag differences on the wings during a yawing motion. Consequently, the yawing damping is increased. The rolling mode gets slightly slower in icing condition and moves towards the origin, which indicates higher aerodynamic damping of the rolling motion.

$$\begin{aligned} \mathrm{EV}_{\mathrm{lat}}(\alpha \approx 7.52^{\circ}, \text{iced}) &= \begin{cases} -15.959 + 0.000i \\ -0.890 \pm 3.562i \\ 0.109 + 0.000i \end{cases} \\ \mathrm{EV}_{\mathrm{lat}}(\alpha \approx 7.45^{\circ}, \text{clean}) &= \begin{cases} -15.090 + 0.000i \\ -0.518 \pm 2.908i \\ -0.045 + 0.000i \end{cases} \end{aligned} \tag{7.2a}$$

$$\begin{aligned} \mathrm{EV}_{\mathrm{lat}}(\alpha \approx 2.14^{\circ}, \text{iced}) &= \begin{cases} -26.231 + 0.000i \\ -1.305 \pm 5.530i \\ 0.034 + 0.000i \end{cases} \\ \mathrm{EV}_{\mathrm{lat}}(\alpha \approx 2.14^{\circ}, \text{clean}) &= \begin{cases} -26.562 + 0.000i \\ -0.791 \pm 4.552i \\ -0.067 + 0.000i \end{cases} \end{aligned} \tag{7.2b}$$

7.2 Simulation Results

This section presents the simulation results for the test runs presented in chapter 6. This includes simulation results for both the single robust -and gain-scheduled controller performance test and a comparison between the two controllers. It also includes different simulation results from scenarios involving de-icing and wind conditions. Overshoot and settling time is used as measures for controller performance. When considering the settling time of a step response, an error band with the size of acceptable steady-state error needs to be defined. For a low-level inner-loop controller, this threshold error needs to be chosen small enough such that the error can easily be corrected by the outer-loop guidance controller. Here, the settling time is the time from step input until the controlled variable stays within the acceptable error band of the final step reference value. The variables shown for the longitudinal and lateral test runs are the controlled variables roll angle, pitch angle and airspeed together with their corresponding control variables aileron deflection, elevator deflection and throttle. In addition, the angle of attack is shown for completeness.

7.2.1 Single Robust Controller

This subsection presents the simulation results from the performance test of the single robust controller. A detailed description of this test run can be found in section 6.1. The longitudinal test run is shown in figure 7.2.

Figures 7.2a and 7.2b shows the pitch angles and the elevator deflections, which are the primary testing variables for this test run. For all types of input signals (ramp with slow/fast

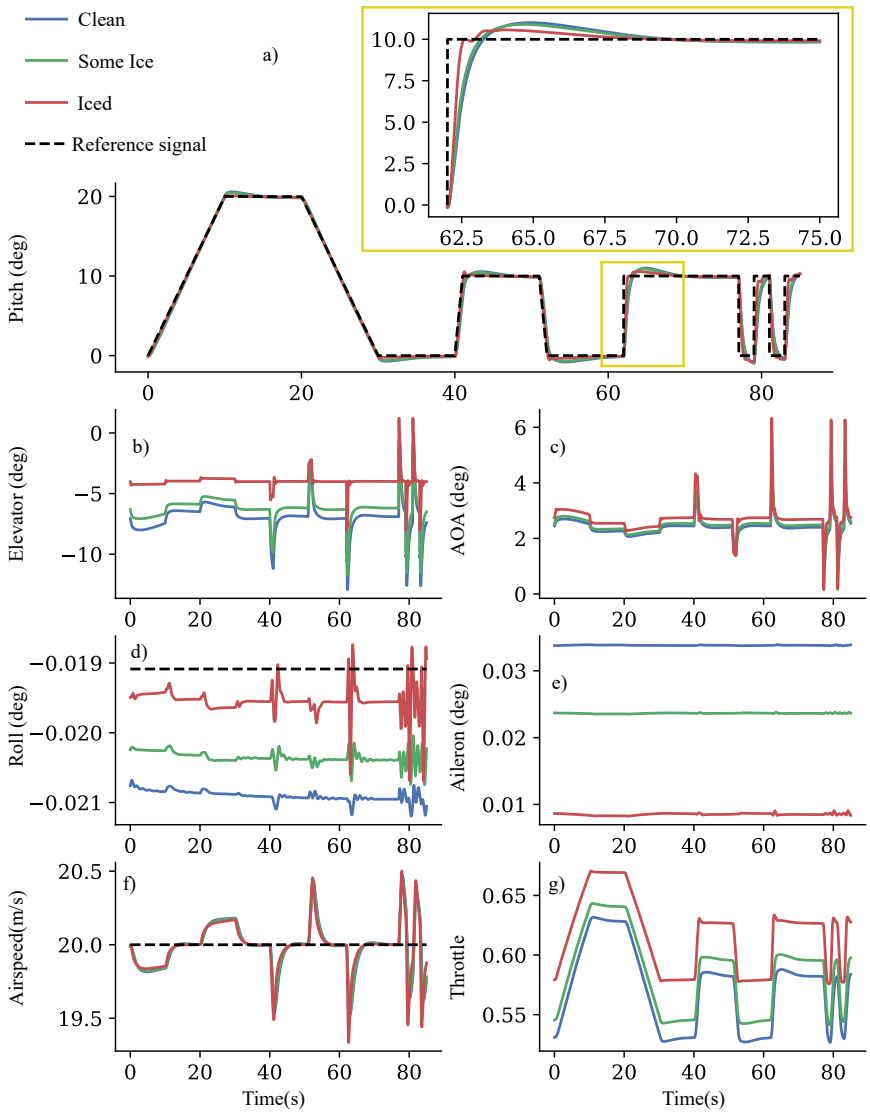

Figure 7.2: Single robust controller longitudinal test run.

rates and step), there is a small overshoot at all tested icing levels. This overshoot tends to decrease when the icing level increases. By looking at the step-input after 62 seconds, which is the step response showed in the zoomed plot in figure 7.2a, the overshoots are 10.0 %, 9.0 % and 5.7 % for icing levels $\zeta = 0$, $\zeta = 0.3$ and $\zeta = 1.0$ respectively. By using an acceptable error band of ± 3 %, the settling times measured from the step at 62 seconds also tend to decrease as the icing level increases. The settling times are 8.11, 7.74 and 6.31 seconds for icing levels $\zeta = 0$, $\zeta = 0.3$ and $\zeta = 1.0$ respectively. The

spikes in elevator deflections correspond to the commanded pitch. Here, it is clear that the control effort is very dependant on the rate of the commanded change. The step responses have considerable larger spikes than the ramp inputs. Also, the spike on the fast is a lot larger than for the slow rate ramp input. Figure 7.2c shows the angle of attack during this simulation. Rapid changes in pitch angle lead to spikes in the angle of attack. This effect seems to be largest for positive step inputs.

Figure 7.2d and 7.2e shows the roll angle and aileron deflection, respectively. For all cases of ice, the roll angle tends to drift slowly away from the reference signal. This effect decreases with rising icing level. However, this is on a very low scale. For all cases, this error is less than 0.002 degrees for a simulation time greater than 80 seconds. Hence, this is negligible and can easily be corrected by a higher-level guidance control loop. Other than this, the lateral directional variables do not depend on the longitudinal control, which is a direct result of the longitudinal/lateral decoupling assumption made in the modelling section 2.1.

Figures 7.2f and 7.2g show the airspeeds and throttle inputs. The airspeed varies between 19.5 and 20.5 seconds. As previously mentioned, the airspeed and pitch angle is strongly coupled, and hence the change in pitch angle is easily viewed on the changes in airspeed. As for the spikes in elevator deflection, a more rapid change in pitch angle gives a greater impact on the airspeed. When the pitch increases, the airspeed decrease and when pitch decreases, the airspeed increases. The airspeed controller tries to keep a constant airspeed at 20 m/s. This explains the shape of the throttle signal. In addition, increased ice leads to increased drag which requires a higher throttle signal to maintain airspeed. This explains why the throttle increases in magnitude when the icing level increases.

Figure 7.3 shows the lateral test run. Figures 7.3a and 7.3b show the roll angle and aileron, which are the primary variables for this test run. For all types of input signals, there is an overshoot at all tested icing levels. As opposed to the longitudinal case, the overshoots at clean and some ice cases are quite similar, and the overshoot at the iced case is larger. By looking at the step-input after 50 seconds (the step response in the zoomed plot in figure 7.3a), the overshoots are 22.9 %, 21.7 % and 25.9 % for icing levels $\zeta = 0$, $\zeta = 0.3$ and $\zeta = 1.0$ respectively. Here, the second-order filter with a maximum acceptable overshoot of 30 % was used in the tuning process from chapter 5. Hence, a quite large overshoot is as expected. A high rate of change in roll angles leads to spikes in the aileron deflection. This is the same behaviour as seen for the pitch angle in the longitudinal case. By using acceptable error band of 3 %, the settling times are found to be 2.90, 2.93 and 3.03 seconds for icing levels $\zeta = 0$, $\zeta = 0.3$ and $\zeta = 1.0$.

7.3c shows the angle of attack. This varies between 2.4 and 4.1 degrees during the test run. When the aircraft goes from a level flight in trim conditions to turning, the absolute value of the velocity component along the body frame z-direction will increase, which can be observed as an increase in the angle of attack. As expected, the direction of turn does not matter on the changes in the angle of attack. The variations increase when the icing level increases. Figures 7.3d and 7.3e show the pitch angle and elevator deflection. The pitch angle is between 0 and 4 degrees for the whole test run. The commanded pitch angle is constant at 2.14 degrees, which is at trim conditions for the given airspeed. However, the

variations in pitch angle need to be looked at in combination with the airspeed and throttle in figures 7.3f and 7.3g. Change in roll angle leads to change in airspeed. Note that these changes are quite small (± 0.06 m/s).

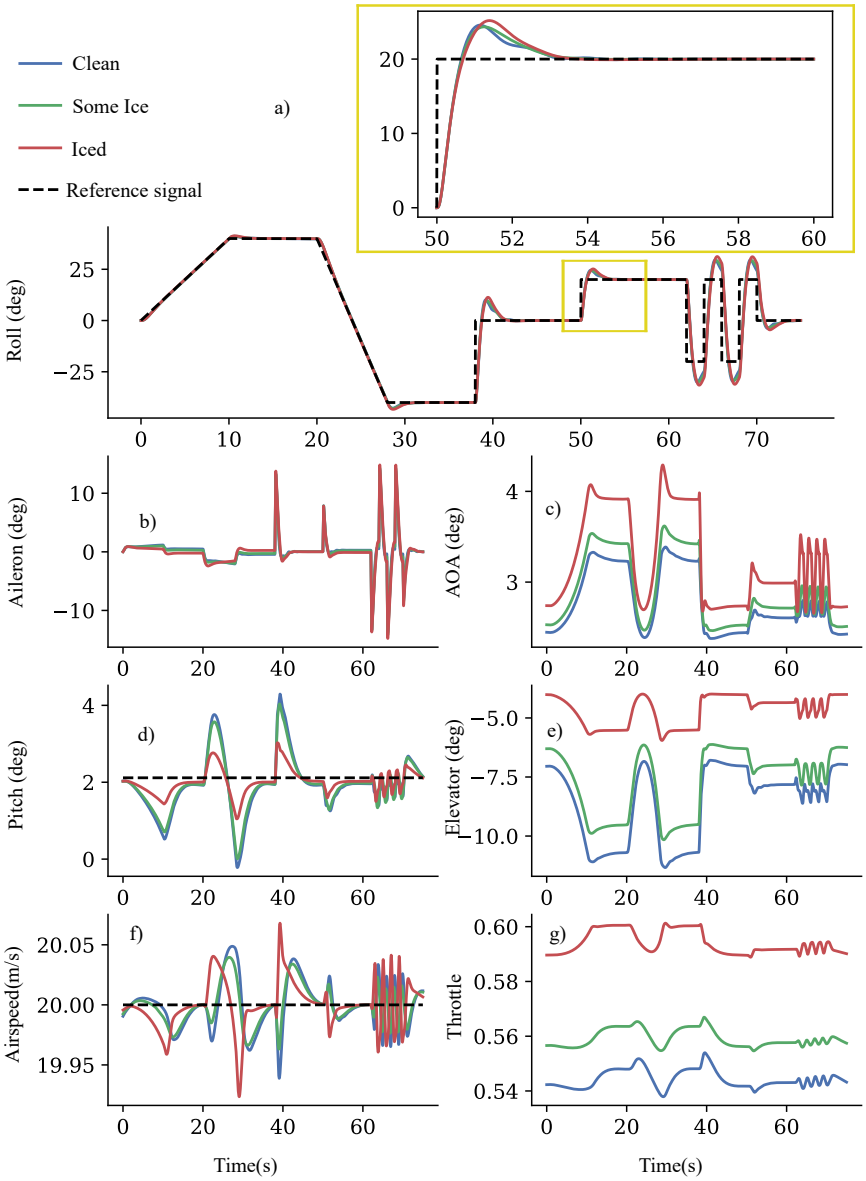

Figure 7.3: Single robust controller lateral performance test run.

7.2.2 Gain-scheduled Controller

The simulations are repeated using the gain scheduled controllers summarized in tables 5.1 and 5.3. The simulation results for the longitudinal test run is shown in figure 7.4. Figures 7.4a and 7.4b show the pitch angles and the elevator deflections. As for the single robust controller there is a small overshoot at all tested icing levels. The tendency of lower overshoot when the icing level increases can also be observed for the gain-scheduled controllers. By looking at the step-input after 62 seconds (this is the step response showed in the zoomed plot in figure 7.4a), the overshoots are 8.0 %, 6.6 % and 4.3 % for icing levels $\zeta = 0$, $\zeta = 0.3$ and $\zeta = 1.0$ respectively. Then, by using acceptable error band of $\pm 3\%$, the settling times (measured from the step at 62 s) are found to be 7.38, 7.00 and 5.26 seconds for icing levels $\zeta = 0$, $\zeta = 0.3$ and $\zeta = 1.0$.

Figures 7.2d and 7.2e show the roll angle and aileron deflection, respectively. The slow drift from the constant reference signal in roll angle is slightly smaller in the gain-scheduled case than it was in the single robust controller case. This effect still tends to decrease with rising icing level. However, this is on a very low scale. For all cases, this error is less than 0.02 degrees for a simulation time greater than 80 seconds. This drift also seems to decay as time goes and go towards a constant steady-state deviation. Figures 7.2f and 7.2g show the airspeeds and throttle inputs. The airspeeds and throttle are almost identical to the single robust controller case.

Figure 7.5 shows the lateral test run with gain-shceduled controllers. Figures 7.5a and 7.5b show the roll angle and aileron. As for the single controller case, there is an overshoot for all icing levels. Here, the overshoot for all icing levels is quite similar. By looking at the step-input after 50 seconds, which is the step response in the zoomed area in figure a, the overshoots are 28.1 %, 28.0 % and 28.5 % for icing levels $\zeta = 0$, $\zeta = 0.3$ and $\zeta = 1.0$ respectively. By again using an acceptable error band 3 %, the settling times are found to be 2.63, 2.30 and 2.28 seconds for icing levels $\zeta = 0$, $\zeta = 0.3$ and $\zeta = 1.0$.

Figure 7.5c shows the angle of attack, figure 7.5d shows the pitch angle, figure 7.5e shows elevator deflection, figure 7.3f shows airspeed and figure 7.3g shows throttle input. All these responses are quite similar to the single robust controller case. However, it is clear that the lateral controller gives more aggressive manoeuvres, leading to a higher degree of dependency between longitudinal and lateral directions. Hence, the spikes in pitch angles are slightly larger in the gain-scheduled case.

7.2.3 Controller Comparison

The performance results on the step responses for gain-scheduled and single robust controllers are summarized in figure 7.6. Here, the two performance measurements, percentage overshoot and settling time, are plotted in a scatter plot. The points marked with filled triangles are from the single robust controller, and the points marked with filled circles are from the gain-scheduled controller. The colour codes show the icing level, where blue is clean, green is partial iced and red is iced. For the longitudinal controllers, both the settling times and overshoot improved by using gain-scheduling for all icing levels. It is worth noticing that the largest difference in settling time is at icing level $\zeta = 1.0$, and is less than 1.5 seconds. The largest difference overshoot is at icing level $\zeta = 0.3$ and is less

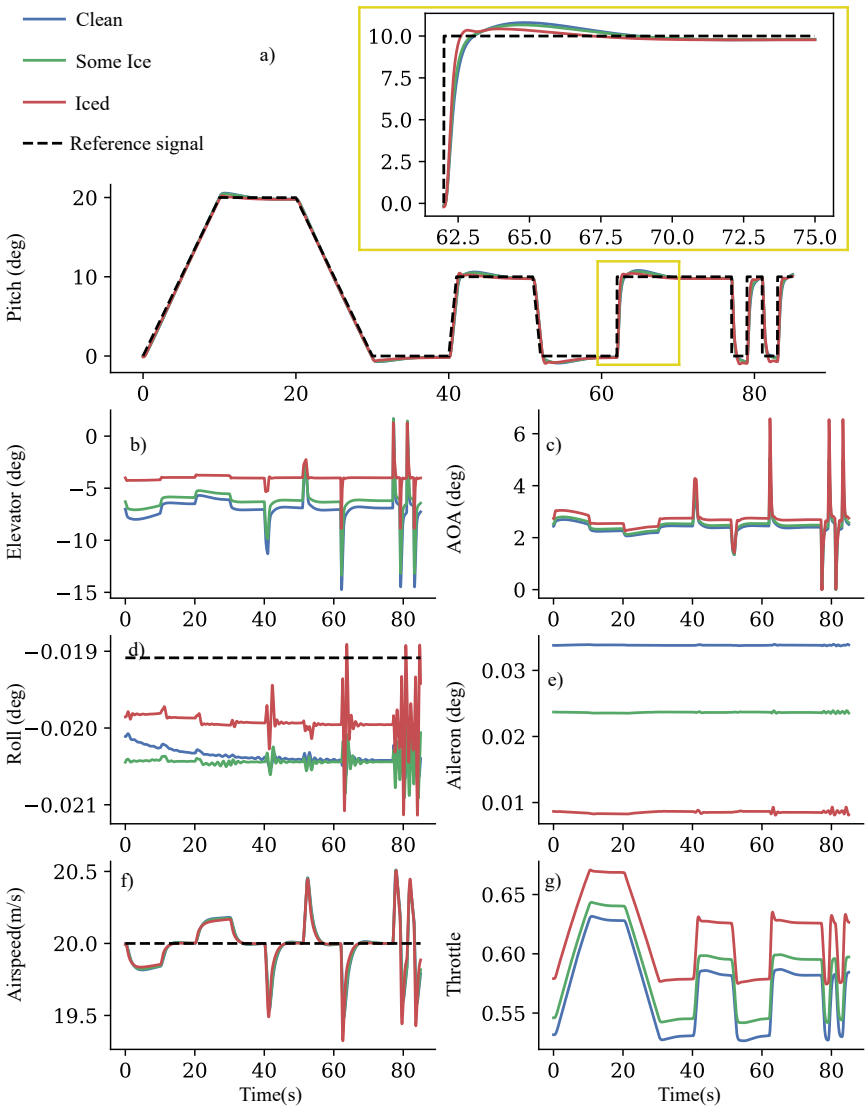

Figure 7.4: Gain-scheduled controller longitudinal test run.

than 2.5 %. In the lateral case, the overshoot is considerably higher for the gain-scheduled case. However, accepted overshoot is a controller design choice. The high accepted overshoot is here made to lower the settling time and increase the ability to reject disturbances. The largest difference in settling time between gain-scheduled and single robust controller is at icing level $\zeta = 1.0$ and is at 2.64 seconds. The largest difference in overshoot is at icing level $\zeta = 0.0$ and is 7.3 %.

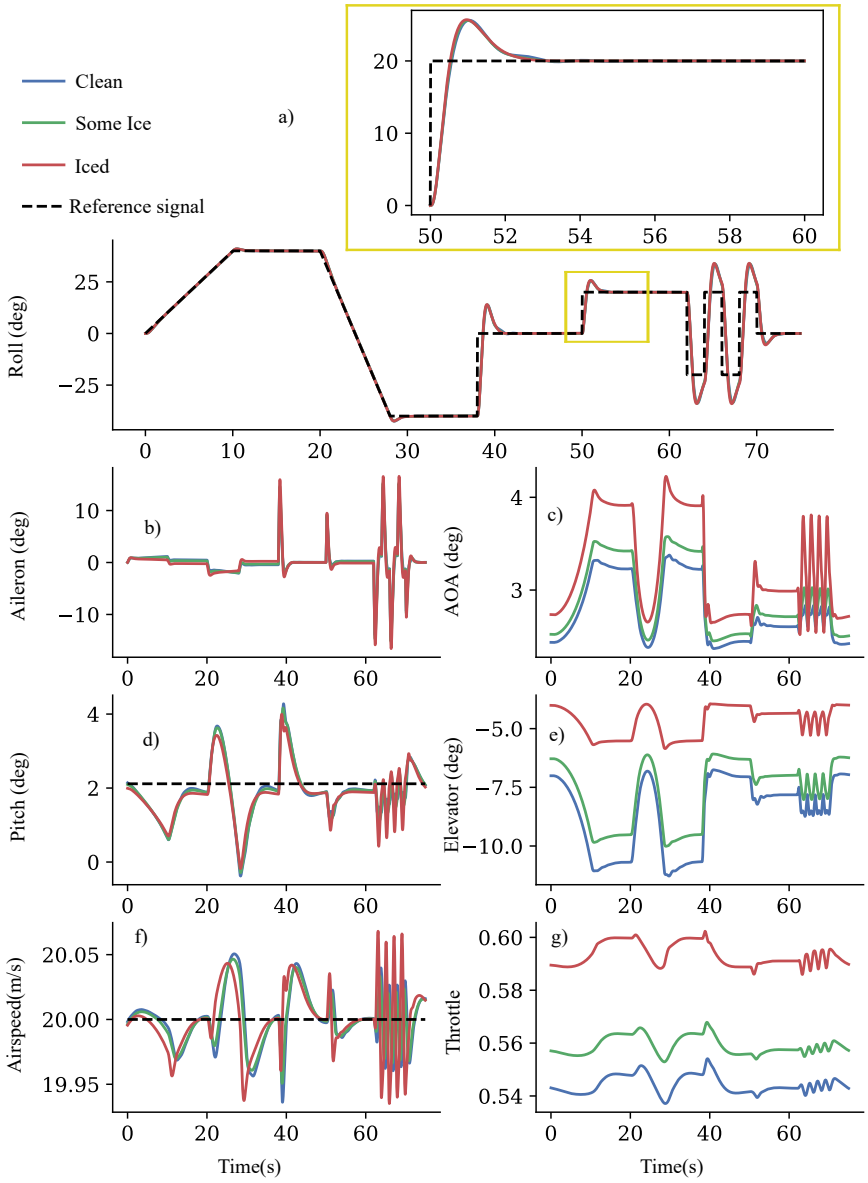

Figure 7.5: Gain-scheduled controller lateral test run.

7.2.4 Wind Conditions

The wind condition simulation case is simulated for both gain-scheduled and single robust controller. Figure 7.7 shows the simulation results for icing level $\zeta = 1.0$. Figures 7.7a and 7.7b show the controlled variables roll and pitch, with their corresponding control signals in figure 7.7c and 7.7d. The angle of attack is shown in figure 7.7c. Airspeed and throttle

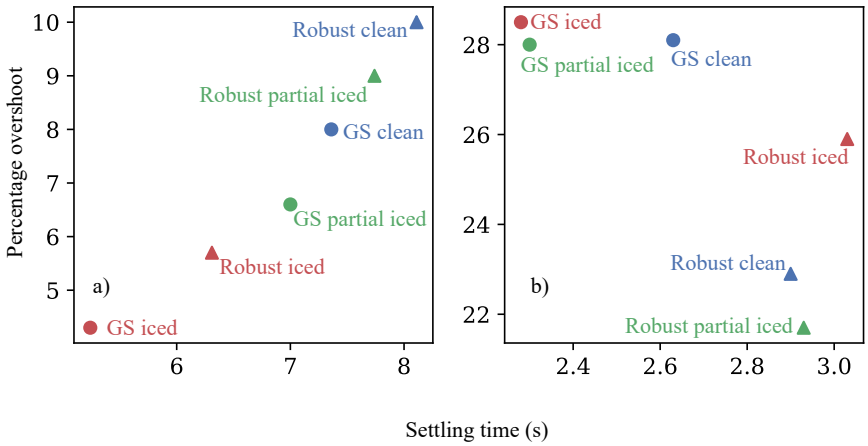

Figure 7.6: *a)* performance for longitudinal direction and *b)* performance lateral direction.

are shown in figures 7.7f and 7.7g. As seen here, both controllers have a quite similar disturbance response. In order to quantify the ability to reject wind gust disturbances, the integral of the absolute value of the error is introduced. Mathematically, this is written as in equation 7.3.

$$\text{ie} = \int_{t_0}^{t} |e(t)|dt \tag{7.3}$$

This quantity is used for comparing the disturbance rejection between the two controllers. For the longitudinal case, the integral errors are 42.31 and 25.28 for the gain-scheduled and single robust controller, respectively. In other words, the disturbance rejection is slightly better for the single robust longitudinal controller than for the gain-scheduled longitudinal controller. For the lateral case, the integral errors are 105.72 and 109.28 for the gain-scheduled and single robust controller, respectively.

7.2.5 Icing Conditions

Due to certain difficulties related to instant changes in the scheduling variable for gain-scheduled controllers using classical switching mechanisms, the icing condition simulation cases are only simulated for the single robust controller. These problems are addressed in chapter 8. Figure 7.8 shows roll- and pitch angle for the first test run described in section 6.3 simulated at trim conditions with airspeed at 21.4 m/s. The aircraft illustrations on the top line of figure shows the icing level of the aircraft at each case. Case 1 is iced on both wings ($\zeta_{\text{left}} = 1$ and $\zeta_{\text{right}} = 1$), case 2 is clean on both wings ($\zeta_{\text{left}} = 0$ and $\zeta_{\text{right}} = 0$), case 3 is iced on both wings ($\zeta_{\text{left}} = 1$ and $\zeta_{\text{right}} = 1$), case 4 is clean on left wing and partially iced on right wing ($\zeta_{\text{left}} = 0$ and $\zeta_{\text{right}} = 0.5$) and finally case 5 is clean on both wings ($\zeta_{\text{left}} = 0$ and $\zeta_{\text{right}} = 0$). All transitions between cases happens instantaneously.

As expected, the roll angle is not noticeably affected by the symmetric change in ice after

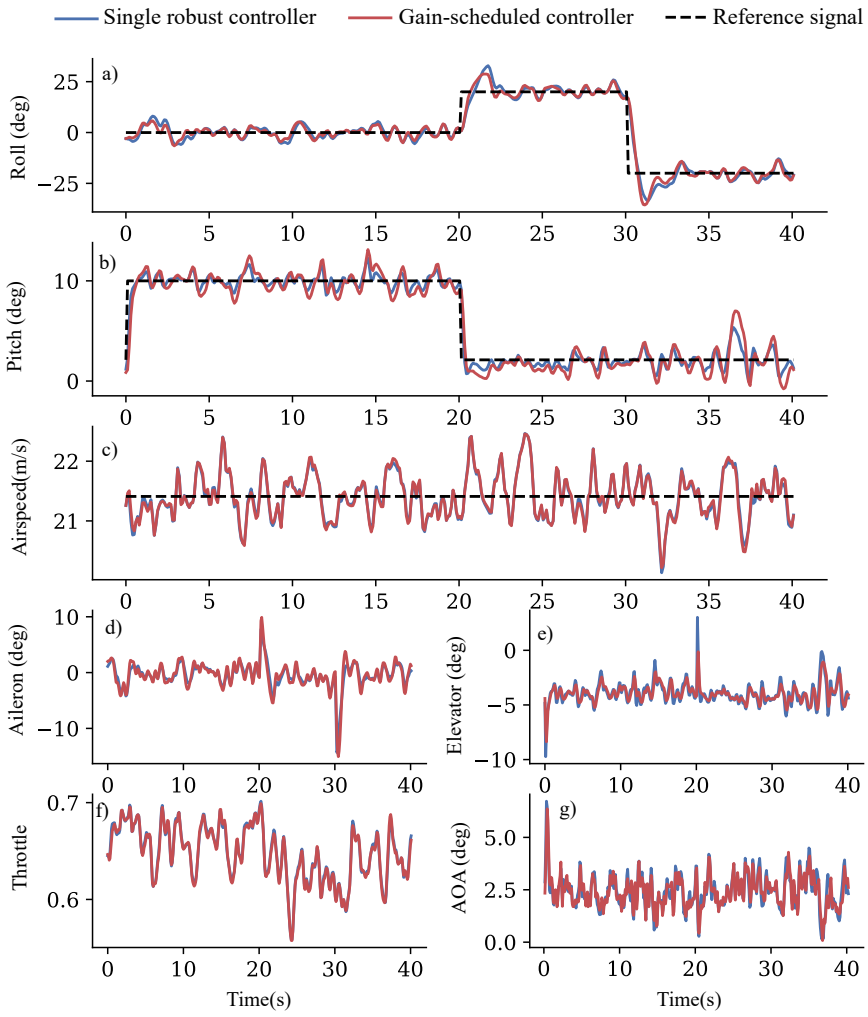

Figure 7.7: Gain-scheduled and single robust controller wind condition test run.

3 seconds. The roll angle is, however, very sensitive to the asymmetric icing disturbances after 20 and 30 seconds. This gives a disturbance response with a deflection at 10 degrees and a slightly oscillatory decay back to the reference value within 4 seconds. The pitch angle is highly dependant both symmetrical and asymmetrical change of icing level. The disturbance response of the pitch angle is slower. The maximum error deflection occurs when the icing level goes from clean to worst-case mixed ice at 20 seconds. This error peak is at approximately 2 degrees. The disturbance response goes slowly back to the reference value within 10 seconds. The steady-state error is less than 0.3 degrees.

The first test run is simulated at trim conditions at different airspeed. Figure 7.9 shows the deflection angle for the transitions between the cases defined in figure 7.8 as a function

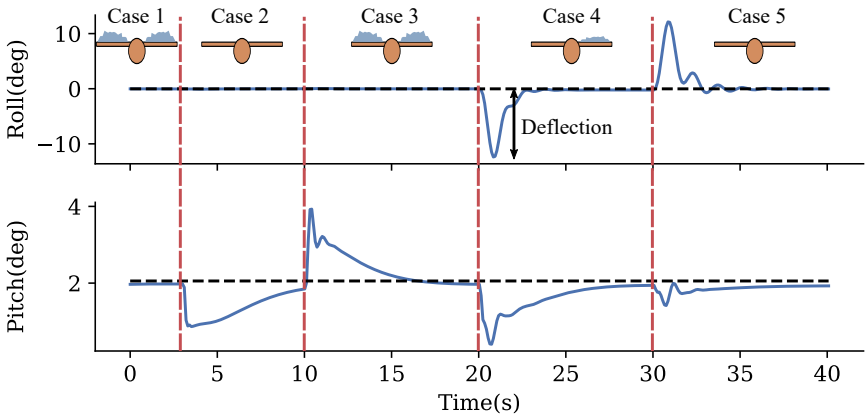

Figure 7.8: De-icing test run

of airspeed. The simulations performed with airspeed at 14, 16, 18, 21 and 24 m/s. The purpose here is to look at how the de-icing procedure is affected by airspeed. Hence, the ice accretion case transition between case 2 and 3 is excluded from this figure. The tendency is quite clear; the disturbance deflection for both pitch angle and roll angles tend to decay when the airspeed rises. This rate of this decay gets smaller for higher airspeeds. For the lateral case in asymmetric icing, the deflection seems to go towards a constant when airspeed gets large, while for the longitudinal case, the deflection seems to go towards 0.

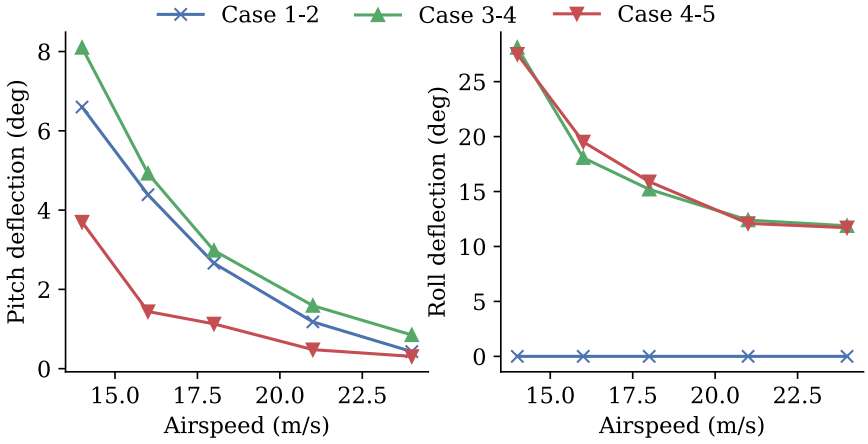

Figure 7.9: Comparison of de-icing deflections at different airspeed

Figure 7.10 shows the second test run described in section 6.3. This test run simulates a short performance test while the aircraft is in asymmetric condition. As expected, the cross-coupling between longitudinal and lateral direction is increased with asymmetric icing. This can be seen in how the aerodynamic coefficients in the lateral direction depend on drag and lift force in figure 4.1. By looking at the roll angle when a step is applied to

the pitch angle, e.g. after 10 seconds, the cross-coupling between longitudinal and lateral direction is increased from the symmetric performance test. The pitch does also depend on the roll angle, but to a lower degree. This can be seen by looking at the pitch angle in figure 7.10b when a step is applied to the roll angle. Figures 7.10c and 7.10d show the icing level on the left and right-wing respectively. Figures 7.10e and 7.10f show the aileron and elevator deflection. When subject to asymmetric icing, a significant aileron control effort is needed to keep the aircraft on a level flight. Given the flight configuration in this test run, the aileron deflection required to maintain level flight is about 10 degrees. Hence, asymmetric icing limits the ability to perform aggressive lateral manoeuvring and can easily cause saturation of the control signal. The saturation limit of the control signal will also give an upper threshold to the degree of asymmetry that can be handled by the UAV. Figures 7.10g and 7.10h show the airspeed and throttle.

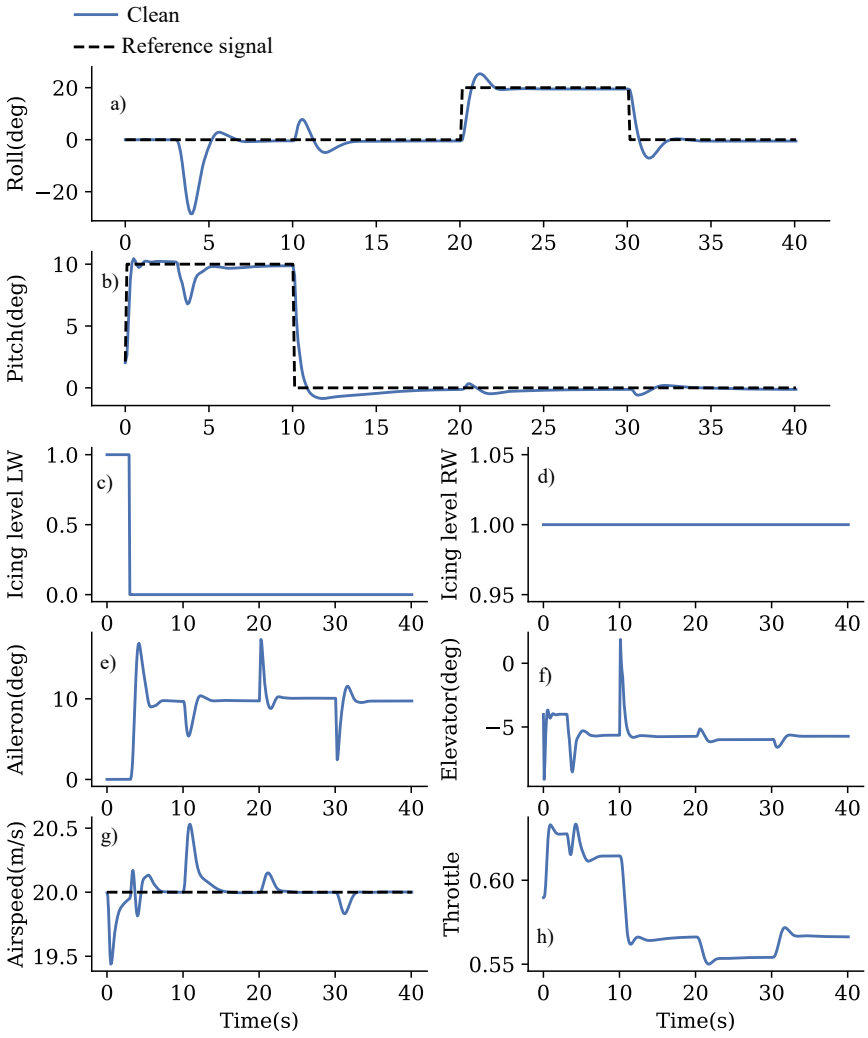

Figure 7.10: Performance test run with asymmetric icing

Chapter 8

Discussion

This chapter will discuss the results presented in chapter 7, and look at some of the challenges related to the controller designs.

8.1 Tuning Approach

As mentioned in chapter 5, there are several trade-offs related to this particular control problem. The controller needs to take the performance and robustness of different plants at different icing levels into account, which makes the tuning problem quite complex. In addition to the general trade-off between performance and robustness for a single plant, there is also a trade-off between performances of plants for different levels of icing, $\zeta \in [0, 1]$. Any mathematical model of a physical system will never be a true representation of a system, and hence all the plants should have a minimum level of robustness. There are several factors that are not included in the icing model [3]. This includes the surface quality of the wings, thermal conductivity, the structural composition of the wing, etc. This emphasizes the importance of robustness to model uncertainties. The tuning approach that was used in this thesis was to define an absolute lower limit of closed-loop robustness and stabilization requirements, and then the performance of the plants of clean and worst-case ice was improved through an iterative process by increasing the closed-loop bandwidth. The robustness requirements were chosen based on the literature and not compared to the magnificence of unmodeled dynamics in this specific model.

8.2 Longitudinal and Lateral Decoupling

The controller method implemented is based on a linearized model where the longitudinal and lateral dynamics are decoupled. The simulation results show that there is a weak coupling, which is illustrated by investigating the roll angle in the longitudinal test run and the pitch angle in the lateral test run. The results indicate that this coupling increases for more aggressive manoeuvres. The simulation model itself is based on a degree of lon-

gitudinal/lateral decoupling. Hence, the cross-coupling between longitudinal and lateral direction will probably be larger in real life than it is in this simulator.

8.3 Gain-scheduling Challenges

Based on the comparison, the gain-scheduled controller undoubtedly improves the performance compared to the single robust controller for all cases of ice. During the simulations, the icing level is assumed known. One of the drawbacks of this controller is that it requires a method to measure the level and type of ice. In general, this is a quite difficult quantity to measure. In addition, classical gain-scheduling methods usually suit best on slow varying variables. This allows switching mechanisms that do not include additional transients to the system. For instance, a switching method can be based on interpolating between controllers. This method would solve the problems for ice accretion, but for the de-icing scenario, where the icing levels instantaneous changes. However, there are more modern scheduling techniques that solve problems related to rapidly varying quantities [33], but these are not implemented and tested in this thesis.

8.4 Dynamic Mode Analysis

The dynamic mode analysis performed in this thesis is based on system analysis from the thoroughly tested FCAT software. These results do not match the eigenvalue analysis done by Winter in [3]. The most alarming difference is that the phugoid mode becomes unstable at both high ($\alpha = 8°$) and low ($\alpha = 2°$) for mixed ice in the analysis done by Winter. This is a fundamental difference from what is seen here. However, the qualitative icing influence on the phugoid mode seen in this thesis seems to be a result of the characteristic change in drag-to-lift ratio. This is similar to observations made in the eigenvalue analysis for larger aircraft [15]. It should be emphasized that the icing model for the Skywalker X8 used in this thesis is based on linear interpolation between the worst-case mixed ice configuration and the base clean aircraft. Hence, aircraft data on different icing configurations than the worst case mixed ice and the base clean aircraft is not available. Therefore, analysis on intermediate icing levels using linear interpolation may give inaccurate results.

8.5 De-icing

From the simulation results on in-flight de-icing, the disturbance effects from de-icing on the aircraft decays with increasing airspeeds. This is consistent with the icing influence on the aircraft aerodynamics seen in section 4.2.4. The simulations are performed at trim conditions at different airspeeds. Generally, higher airspeed at level-flight leads to a lower angle of attack. The deflection angles caused by the icing disturbance is reduced when the difference in aerodynamic moment coefficients between the two cases is lower.

The difference in pitch moment coefficients between clean and iced icing configuration is at its lowest point for low angles of attack in the area of about 0 degrees. For one angle of attack, the pitch moment coefficient is equal for the clean and iced case. This explains why the angular disturbance deflection goes towards 0 degrees when airspeed gets large.

The difference in roll moment coefficients between clean and iced icing configuration

decreases for low angles of attack. However, the difference is at its lowest for negative angles of attack. Hence, when the angle of attack goes towards zero as airspeed gets large, the deflection angles for the roll motion when de-icing will go towards a constant and not zero.

Chapter 9

Conclusion

The main goal of this thesis was to develop inner-loop controllers for a fixed-wing UAV with robust performance. A software package was developed to analyze the aircraft system, tune controllers and perform simulations. Successful simulation tests demonstrated both the feasibility and the performance of the controller in wind and icing conditions.

Two types of inner-loop controllers based on H_∞ optimal control were implemented and tested; a single robust controller and a gain-scheduled controller. In order to mitigate the effects of icing, both controllers fulfilled closed-loop requirements to ensure stability and robustness to model uncertainty. The simulation results showed that both controller types gave satisfactory results in terms of robustness, stability and performance. From the performance comparison of the two controller types, one can conclude that by increasing the information available and assuming that the level of icing is known, the performance in terms of settling time and overshoot is improved by using a gain scheduled controller.

The influence of icing on dynamic aircraft modes was analyzed. How the Skywalker X8 dynamics is affected by icing conditions was investigated based on a simulation model where icing is modelled using linear interpolation between base aircraft without ice and the worst-case mixed ice configuration. Due to limited available data for different icing configurations of the Skywalker X8, it is not possible to make a general conclusion of the influence of different icing configurations on the dynamic modes based on analysis in this thesis. Nevertheless, the typical change of aerodynamic behaviour in icing conditions, such as increased drag, can be seen as changes in particular dynamic modes characteristics.

In-flight de-icing was performed using the single robust controller for different levels of airspeed. The tendency was clear; higher airspeed within the tested range of reasonable UAV airspeeds minimizes the disturbance related to instantaneous removal of ice.

9.1 Future Work

An important step in the further development of the control system for the Skywalker X8 in icing condition is to improve the accuracy of the mathematical model of icing for the Skywalker X8. This can, for instance, be done by performing Computational fluid dynamics (CFD) simulations for different icing configurations. Then, a dynamic mode analysis for intermediate icing configurations could give a more conclusive analysis than the one shown in this thesis.

The same principle yields in the asymmetric icing case. While the model deduction performed in this thesis illustrates the effect of asymmetric flight, it is based on several assumptions which may lead to inaccuracies compared to real flight. Hence, performing a CFD analysis on isolated wings with different icing configurations and identify the new aerodynamic coefficients would improve the model accuracy.

As discussed, it would also be interesting to implement appropriate switching mechanisms for the gain-scheduled controllers and verify if it is possible to improve the disturbance response when subject to de-icing. The systematic tuning methods proposed in this thesis proved to be well functioning in the simulator. Future work should include testing the inner-loop controllers in combination with an outer guidance loop in real life flight test experiments.

Bibliography

[1] R. Kleiven, "Robust and gain scheduled flight control of fixed-wing UAVs in icing conditions", unpublished, 2020.

[2] S. K. Thomas, R. P. Cassoni and C. D. MacArthur, "Aircraft anti-icing and de-icing techniques and modeling", *Journal of aircraft*, vol. 33, no. 5, pp. 841–854, 1996.

[3] A. Winter, "Systems identification, flight performance, and control of a fixed-wing UAV in icing conditions",

[4] G. H. Elkaim, F. A. P. Lie and D. Gebre-Egziabher, "Principles of guidance, navigation, and control of uavs", *Handbook of Unmanned Aerial Vehicles*, pp. 347–380, 2015.

[5] R. W. Beard and T. W. McLain, *Small unmanned aircraft: Theory and practice*. Princeton university press, 2012.

[6] E. Lavretsky and K. A. Wise, "Robust adaptive control", in *Robust and adaptive control*, Springer, 2013, pp. 317–353.

[7] J. P. How, E. Frazzoli and G. V. Chowdhary, "Linear flight control techniques for unmanned aerial vehicles", in *Handbook of unmanned aerial vehicles*, Springer Netherlands, 2015, pp. 529–576.

[8] K. Gryte, R. Hann, M. Alam, J. Rohac, T. A. Johansen and T. I. Fossen, "Aerodynamic modeling of the Skywalker X8 Fixed-Wing Unmanned Aerial Vehicle", *2018 International Conference on Unmanned Aircraft Systems, ICUAS 2018*, pp. 826–835, 2018. DOI: 10.1109/ICUAS.2018.8453370.

[9] R. W. Gent, N. P. Dart and J. T. Cansdale, "Aircraft icing", *Philosophical Transactions of the Royal Society of London. Series A: Mathematical, Physical and Engineering Sciences*, vol. 358, no. 1776, pp. 2873–2911, 2000.

[10] T. Cebeci and F. Kafyeke, "Aircraft icing", *Annual review of fluid mechanics*, vol. 35, no. 1, pp. 11–21, 2003.

[11] R. Hann, A. Wenz, K. Gryte and T. A. Johansen, "Impact of atmospheric icing on UAV aerodynamic performance", in *2017 Workshop on Research, Education and Development of Unmanned Aerial Systems (RED-UAS)*, 2017, pp. 66–71. DOI: 10.1109/RED-UAS.2017.8101645.

[12] A. Heinrich, R. Ross, G. Zumwalt, J. Provorse and V. Padmanabhan, "Aircraft icing handbook. volume 2", Gates Learjet Corp Wichita KS, Tech. Rep., 1991.

[13] C. Deiler, "Aerodynamic modeling, system identification, and analysis of iced aircraft configurations", *Journal of Aircraft*, vol. 55, no. 1, pp. 145–161, 2018.

[14] C. Deiler and T. Kilian, "Dynamic aircraft simulation model covering local icing effects", *CEAS Aeronautical Journal*, vol. 9, no. 3, pp. 429–444, 2018.

[15] C. Deiler, "Comparison of flight characteristics of two different airplanes and ice configurations", *Journal of Aircraft*, vol. 57, no. 5, pp. 995–1000, 2020.

[16] R. Hann, "Atmospheric ice accretions, aerodynamic icing penalties, and ice protection systems on unmanned aerial vehicles", 2020.

[17] G. Chowdhary, E. N. Johnson, R. Chandramohan, M. S. Kimbrell and A. Calise, "Guidance and control of airplanes under actuator failures and severe structural damage", *Journal of Guidance, Control, and Dynamics*, vol. 36, no. 4, pp. 1093–1104, 2013.

[18] R. Kleiven, *Flight control analysis toolbox*, https://github.com/rukleiven/fcat, 2021.

[19] M. V. Cook, *Flight dynamics principles: a linear systems approach to aircraft stability and control*. Butterworth-Heinemann, 2012.

[20] "Flying qualities of piloted airplanes", 1980, U.S. Military Specification MIL-F-8785C.

[21] *MathWorks dryden wind turbulence model (continuous)*, https://se.mathworks.com/help/aeroblks/drydenwindturbulencemodelcontinuous.html, Accessed: 5/22/2021.

[22] G. Vinnicombe, *Uncertainty and Feedback: H [infinity] Loop-shaping and the [nu]-gap Metric*. World Scientific, 2001.

[23] S. Skogestad and I. Postlethwaite, *Multivariable feedback control: analysis and design*. Citeseer, 2007, vol. 2.

[24] K. Glover and J. C. Doyle, "State-space formulae for all stabilizing controllers that satisfy an h-norm bound and relations to relations to risk sensitivity", *Systems Control Letters*, vol. 11, no. 3, pp. 167–172, 1988, ISSN: 0167-6911. DOI: https://doi.org/10.1016/0167-6911(88)90055-2. [Online]. Available: http://www.sciencedirect.com/science/article/pii/0167691188900552.

[25] J. Doyle, K. Lenz and A. Packard, "Design examples using μ-synthesis: Space shuttle lateral axis fcs during reentry", in *Modelling, Robustness and Sensitivity Reduction in Control Systems*, Springer, 1987, pp. 127–154.

[26] K. J. Åström, "Adaptive control", in *Mathematical System Theory: The Influence of R. E. Kalman*, A. C. Antoulas, Ed. Berlin, Heidelberg: Springer Berlin Heidelberg, 1991, pp. 437–450, ISBN: 978-3-662-08546-2. DOI: 10.1007/978-3-662-08546-2_24. [Online]. Available: https://doi.org/10.1007/978-3-662-08546-2_24.

[27] K. Zhou and J. C. Doyle, *Essentials of robust control*. Prentice hall Upper Saddle River, NJ, 1998, vol. 104.

[28] J. Steele and G. Vinnicombe, "The ν-gap metric and the generalised stability margin", in *Advanced Techniques for Clearance of Flight Control Laws*, Springer, 2002, pp. 57–75.

[29] K. J. Åström and R. M. Murray, *Feedback systems: an introduction for scientists and engineers*. Princeton university press, 2010.

[30] *Python control systems library*, https://python-control.readthedocs.io/en/0.9.0/, Accessed: 5/22/2021.

[31] A. Winter, R. Hann, A. Wenz, K. Gryte and T. A. Johansen, "Stability of a flying wing UAV in icing conditions", in *8th European Conference for Aeronautics and Space Sciences (EUCASS), Madrid*, 2019.

[32] K. Gryte, "Precision control of fixed-wing UAV and robust navigation in gnssdenied environments", 2020.

[33] D. J. Leith, A. Tsourdos, B. White and W. Leithead, "Application of velocity-based gain-scheduling to lateral auto-pilot design for an agile missile", *Control Engineering Practice*, vol. 9, no. 10, pp. 1079–1093, 2001.

Appendix A

Rotation Matrices

This appendix lists the relevant rotation matrices used in chapter 2.

A.1 Body to Inertial

$$\mathbf{R}_b^i(\phi,\theta,\psi) = \begin{bmatrix} c_\theta c_\psi & s_\phi s_\theta c_\psi - c_\phi s_\psi & c_\phi s_\theta c_\psi + s_\phi s_\psi \\ c_\theta s_\psi & s_\phi s_\theta s_\psi + c_\phi c_\psi & c_\phi s_\theta s_\psi - s_\phi c_\psi \\ -s_\theta & s_\phi c_\theta & c_\phi c_\theta \end{bmatrix} \tag{A.1}$$

Here, $sin(x)$ and $cos(x)$ are written on a compact form s_x and c_x.

A.2 Body to Wind

$$\mathbf{R}_b^w(\alpha,\beta) = \begin{bmatrix} cos(\beta)cos(\alpha) & -sin(\beta)cos(\alpha) & -sin(\alpha) \\ sin(\beta) & cos(\beta) & -sin(\beta)sin(\alpha) \\ -cos(\beta)sin(\alpha) & 0 & cos(\alpha) \end{bmatrix} \tag{A.2}$$

Here, α is the angle of attack, and β is the angle of sideslip.

Appendix B

Skywalker X8 Simulation Parameters

B.1 Aerodynamic Coefficients

Table B.1: Skywalker X8 aerodynamic coefficients

Parameter	Clean	Iced
$C_{D_{\delta_e}}$	0.8461	0.8461
$C_{Y_{\delta_a}}$	−0.0696	−0.0696
$C_{L_{\delta_e}}$	0.5872	0.5872
$C_{\mathrm{l}_{\delta_a}}$	0.2987	0.2987
$C_{\mathrm{m}_{\delta_e}}$	−0.4857	−0.4857
$C_{\mathrm{n}_{\delta_a}}$	0.0076	0.0076
C_{Y_p}	−0.185	−0.034
C_{Y_r}	0.005	0.002
C_{L_q}	4.63	−3.41
C_{D_q}	0	0
C_{l_r}	0.039	0.158
C_{n_p}	−0.027	−0.017
C_{l_p}	−0.409	−0.407
C_{m_q}	−1.99	−2.09
C_{n_r}	−0.022	−0.049

B.2 Physical Measures

Table B.2: Skywalker X8 physical measures

Parameter	Symbol	Value	
Wing span	b	2.1	m
Mean aerodynamic chord	c_M	0.3571	m
Wing area	S_w	0.75	m^2
Area swept by propeller	S_p	0.1018	m^2
Motor constant	k_m	40	
Motor efficiency factor	C_{prop}	1	

Table B.3: Skywalker X8 mass, moments of inertia and products of inertia, based on experimental data from [32]

Parameter	Value	
m	3.3650	kg
I_{xx}	0.340	kgm^2
I_{yy}	0.165	kgm^2
I_{zz}	0.400	kgm^2
I_{xy}	0.000	kgm^2
I_{xz}	-0.031	kgm^2
I_{yz}	0.000	kgm^2

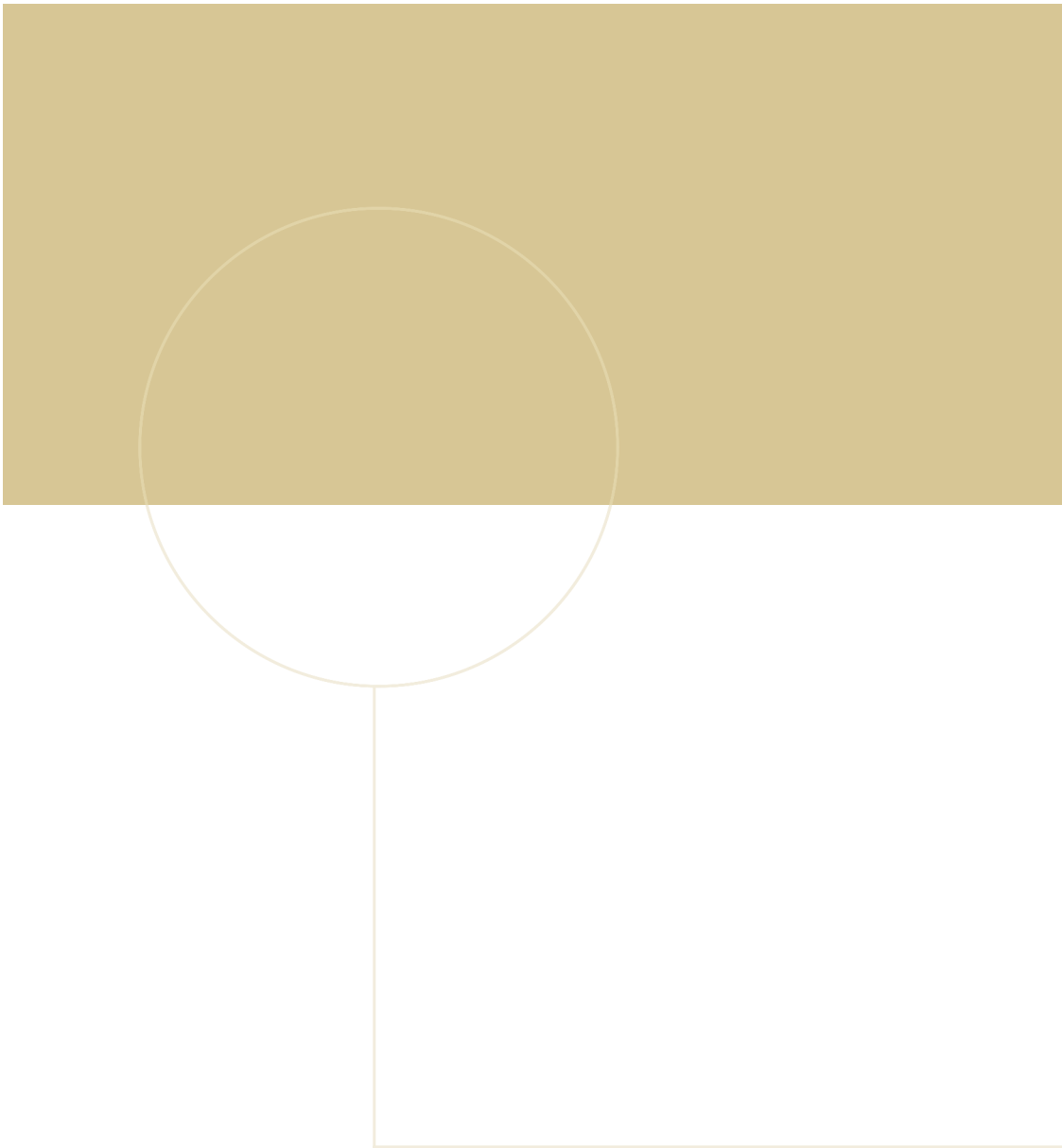

NTNU

Norwegian University of
Science and Technology